CD63 sorts cholesterol into endosomes for storage and distribution via exosomes

Roberta Palmulli, Mickaël Couty, Melissa C Piontek, Maharajah Ponnaiah, Florent Dingli, Frederik J Verweij, Stéphanie Charrin, Matteo Tantucci, Sajitha Sasidharan, Eric Rubinstein, et al.

CD63 sorts cholesterol into endosomes for storage and distribution via exosomes

Roberta Palmulli[1,2*], Mickaël Couty[2,3*], Melissa C. Piontek[4], Maharajah Ponnaiah[5], Florent Dingli[6], Frederik J. Verweij[2], Stéphanie Charrin[7], Matteo Tantucci[2], Sajitha Sasidharan[4], Eric Rubinstein[7], Anatol Kontush[8], Damarys Loew[6], Marie Lhomme[5], Wouter H. Roos[4], Graça Raposo[1,9], Guillaume van Niel[1,2,3,10].

[1] Institut Curie, PSL Research University, CNRS, UMR144, 26 rue d'Ulm, 75248 Paris Cedex 05, France

[2] Université de Paris, Institute of Psychiatry and Neuroscience of Paris (IPNP), INSERM U1266, F-75014 Paris, France

[3] Nantes Université, Inserm UMR 1307, CNRS UMR 6075, Université d'Angers, CRCI2NA, Nantes, France.

[4] Moleculaire Biofysica, Zernike Instituut, Rijksuniversiteit Groningen, 9747 AG Groningen, The Netherlands.

[5] Foundation for Innovation in Cardiometabolism and Nutrition (IHU ICAN), ICAN I/O - data sciences (MP), ICAN omics – lipidomics (ML), 75013 Paris, France

[6] Institut Curie, PSL Research University, Centre de Recherche, CurieCoreTech Spectrométrie de Masse Protéomique, Paris 75248, France

[7] Sorbonne Université, Inserm, CNRS, Centre d'Immunologie et des Maladies Infectieuses, CIMI-Paris, F-75013 Paris, France

[8] National Institute for Health and Medical Research (INSERM), UMR-ICAN 1166, Paris, France

[9] Institut Curie, PSL Research University, CNRS, UMR144, Cell and Tissue Imaging Facility (PICT-IBiSA), 26, rue d'Ulm, 75248 Paris Cedex 05, France

[10] GHU-Paris Psychiatrie et Neurosciences, Hôpital Sainte Anne, F-75014 Paris, France.

* Both authors contributed equally to this work.

Corresponding author: Guillaume van Niel, guillaume.van-niel@inserm.fr

Abstract

Extracellular vesicles (EV) such as exosomes are now recognized as key players of intercellular communication. Their role is influenced by their specific composition in protein and lipid sets that are sorted during their generation as intraluminal vesicles (ILV) in multivesicular endosomes. Here, we report that a key component of small EVs, the tetraspanin CD63, sorts cholesterol to ILVs, generating a pool that can be mobilized by the NPC1/2 complex and exported via exosomes to recipient cells. In absence of CD63, cholesterol is retrieved from endosomes by an actin-dependent vesicular transport, placing CD63 and cholesterol at the center of a balance between inward and outward budding of endomembranes. These results establish CD63 as a lipid sorting mechanism within endosomes and show that ILVs and exosomes are alternative providers of cholesterol.

Introduction

Within the endosomal pathway, coordination of outward and inward membrane remodeling and sorting mechanisms enable the recycling of materials towards the Golgi complex or the plasma membrane[1–3], as well as their packaging into intraluminal vesicles (ILVs) of Multivesicular Endosomes (MVEs)[4,5]. Efficient sorting to ILVs is vital for various cellular functions such as cell signaling and protein catabolism. The composition of ILVs, including proteins and lipids, influences their function post-secretion as exosomes in the extracellular environment[6, 7]. While sorting mechanisms for proteins have been extensively studied[4,8], the mechanisms responsible for enriching specific sets of lipids on ILVs remain poorly understood.

CD63 is a member of the tetraspanin family that organize themselves into lipid microdomains enriched in gangliosides, cholesterol, and a network of partner proteins whose trafficking, cleavage, and functions they regulate[9–11]. Unlike other tetraspanins, CD63 is primarily localized within late endosomes/MVEs, lysosomes, where it is concentrated in ILVs and hence enriched in exosomes[12], making it a reliable marker and tool to label and manipulate this EV subpopulation[13,14]. CD63 is involved in diverse cellular processes, including cargo transport and sorting[15]. Its roles vary depending on the cell type studied; for instance, it regulates the targeting of CXCR4 to endolysosomes in T cells[16] and the clustering of P-selectin at the plasma membrane of endothelial cells[17]. In melanocytes[18] and Epstein–Barr virus (EBV)-infected B cells, CD63 functions as both a cargo[5,19] and a regulator[18] of sorting mechanisms at MVEs[18, 20, 21,22].

Here we investigated whether a primary molecular mechanism would underlie CD63's various roles, by comparing the consequences of CD63 depletion in two different cell lines. The findings reveal a fundamental role for CD63 in sorting cholesterol to ILVs and exosomes. By promoting the accumulation of cholesterol within ILVs, CD63 regulates endosomal membrane remodeling. This pool of stored cholesterol can be retrieved by cells from ILVs and exosomes in a manner dependent on NPC1. Thus, CD63 emerges as a key regulator of cholesterol endosomal sorting, providing alternative sources of cholesterol through ILVs and exosomes.

Results

CD63 does not affect sEV protein composition and secretion

To identify the shared role of CD63, we compared two commonly used cell lines for CD63 research: HeLa[23] and MNT-1[18,20]. Using CRISPR/CAS9, we generated CD63 knockout (KO) HeLa and MNT-1 cells, obtaining two HeLa KO clones (KO#1 and KO#2) and one CD63 KO MNT-1 clone. Western blot analysis of cell lysates confirmed complete CD63 depletion without notable changes in CD9, Alix (both cell types), syntenin (HeLa), or endogenous ApoE (MNT-1) (Fig.1a). Analysis of small extracellular vesicles (sEVs) from wild-type (WT) and CD63 KO cells showed no significant differences in sEV markers (Fig. 1b) except for reduced ApoE levels in CD63 KO MNT-1-derived sEVs, as previously reported[20] .

Nanoparticle tracking analysis (NTA) of sEVs obtained by differential ultracentrifugation (UC) (Fig. 1c) or size exclusion chromatography (SEC) (Fig. 1, Extended Data Fig. 1a) demonstrated similar sEV release and size distribution between WT and CD63 KO cells, consistent across different growth media conditions (Extended Data Fig. 1b,c).

To mitigate potential compensatory mechanisms induced by long-term tetraspanin depletion[24], we performed similar analyses in MNT-1 cells treated with Ctrl siRNA or CD63 siRNA and on sEVs isolated from cells grown in lipoprotein-depleted serum (LPDS)-supplemented media. Partial CD63 depletion by siRNA did not affect cellular and sEV markers or the number and size distribution of sEVs, except for reduced ApoE levels in sEVs (Extended Data Fig. 1d,e). Analysis of endolysosomal compartments revealed comparable patterns between WT and CD63 KO HeLa cells (Fig. 1e,f), in line with unaffected sEV production.

We conducted quantitative mass spectrometry analyses of whole cell membranes from WT or CD63 KO HeLa or MNT-1 cells and corresponding sEVs isolated by SEC (Fig. 2 and Extended Data Fig. 2). CD63 depletion affected the level of a very minute number of proteins in HeLa (Extended Data Fig. 2a,b) or MNT-1 (Extended Data Fig. 2c,d) cell lysates, with no prior

associations with CD63. GO-Term analysis showed proteins enriched in WT MNT1 compared to KO associated with membrane raft and EVs (Extended Data Fig. 2d). On sEVs, several proteins were decreased upon CD63 depletion in HeLa-derived sEVs, including MMP12 that displays similar expression pattern as CD63[25] and the scaffold protein BASP1 that is enriched in EVs thanks to a myristoylated moiety[26], while in MNT-1-derived sEVs, VGF secretion is correlated to VAMP7 dependent CD63 secretion[27] and LGALS3BP can be enriched in sEV overexpressing GFP-CD63[13] but dissociates from EV upon sucrose gradient isolation[26] (Extended Data Fig. 2e-h).

Correlation plot analysis of proteins enriched in WT condition compared to CD63 KO in both HeLa and MNT-1 cell lysates identified CD63 as the only significant change, with no specific associated GO-term (Fig. 2a and 2b). In sEVs, none of the previously identified proteins was commonly depleted from both cell types (Fig. 2c and d) and the ones commonly depleted were not linked to the endolysosomal pathway, with the GO-term mainly revealing enrichment in transmembrane transporter activity.

In summary, CD63 depletion neither affected sEV release nor induced common changes in sEV protein composition or steady-state level of proteins in both cell types. During the publication process, similar findings were confirmed in HEK293[28] and MCF7 cells[29].

CD63 regulates cellular lipid homeostasis

Despite the lack of a clear effect of CD63 depletion on sEV protein composition or number, we turned our focus to other common EV cargo molecules. The enrichment of soluble proteins associated with membrane microdomains in WT sEVs and the specific affinity of tetraspanins for certain lipids such as cholesterol and gangliosides[8,9] prompted us to investigate the influence of CD63 expression on lipid homeostasis. We conducted lipidomic analyses using mass spectrometry of whole cell membranes extracted from HeLa and MNT-1 WT or CD63 KO cells, as well as sEVs/exosomes isolated from the same cells by SEC. To prevent the co-isolation of exogenous lipoproteins with sEVs, cells were cultured in LPDS supplemented media for at least two days before collecting the conditioned media and processing the cells for further analyses.

Lipidomic analysis of sEVs from both HeLa-WT (Fig. 3a and Extended data Fig. 3a) and MNT-1-WT (Fig. 3b and Extended data Fig. 3b) revealed that sEVs predominantly consisted of phosphatidylcholine (PC), phosphatidylethanolamine (PE), plasmalogen PE (PE-P), sphingomyelin (SM), or free cholesterol (FC), consistent with previous reports in other cell types[30,31]. Compared to whole cell lysates, sEVs were enriched in FC, cholesteryl esters (CE),

SM, and PE-P in HeLa cells, while being depleted of bis(monoacylglycerol)phosphate (BMP), phosphatidylinositol (PI), PC, lysophosphatidylglycerol (LPG), and phosphatidic acid (PA) (Fig. 3a). Similarly, sEVs from MNT-1 WT cells were enriched in FC, CE, SM, and lysophosphatidylcholine (LPC), while being depleted in BMP, PC, PE, PI, phosphatidylglycerol (PG), and LPG (Fig. 3b). Notably, FC, CE, and SM were commonly enriched in sEVs from both cell types, suggesting potentially elusive active sorting processes. In contrast, BMP, enriched on intraluminal vesicles (ILVs) of late endosomes[32], and Ceramide (Cer), implicated in ILV formation[33], were not enriched.

CD63 knockout resulted in a slight but significant decrease in FC, Cer, and PE-P in HeLa cells (Fig. 3c and Extended data Fig. 3a), and an increase in PE in MNT-1 cells (Fig. 3d and Extended data Fig. 3b). When comparing isolated sEVs, HeLa CD63 KO sEVs exhibited lower levels of LPG compared with HeLa WT sEVs (Fig. 3e and Extended data Fig. 4a), while MNT-1 CD63 KO showed increased CE levels and decreased PE-P, BMP, lysophosphatidylethanolamine (LPE), and FC levels (Fig. 3f and Extended data Fig. 4b). Additionally, we analyzed the PC to PE molar ratio (PC/PE) in cells and sEVs as a marker of global changes in lipid homeostasis. The ratio was affected by CD63 depletion in sEVs but not in cells in HeLa, and inversely in MNT-1(Extended data Fig. 4c,d).

Overall, lipidomic analyses indicated that upon CD63 depletion, there was a slight modulation of cholesterol homeostasis common to both cell types, suggesting a potential alteration in cholesterol trafficking. As cholesterol directly or indirectly[9,34,35] interacts with tetraspanins and is co-enriched with CD63 on ILVs[36] and sEVs[30], we further investigated the role of CD63 in cholesterol homeostasis at the endosomal level.

CD63 modulates intracellular cholesterol trafficking.

Cholesterol homeostasis in late endosomes and lysosomes has been primarily studied in the context of its delivery to lysosomes via endocytosis of lipoproteins. In endosomal compartments, Niemann-Pick Type C1 and 2 proteins (NPC1 and NPC2) facilitate the translocation of exogenous cholesterol from lipoproteins to the limiting membrane of late endosomes[37]. Cholesterol is then transported to other organelles, mainly the endoplasmic reticulum (ER), via non-vesicular trafficking pathways involving membrane contact sites[37,38].

We initially analyzed the effect of CD63 depletion on the capacity of cells to uptake and process LDL-derived cholesterol. Incubation of WT and CD63 KO HeLa cells with fluorescent LDL (LDL-BODIPY) did not reveal any significant defect in the endocytosis of exogenous cholesterol sources (Fig. 4a). Immunolabeling of cholesterol using the D4 fragment of the

cholesterol-binding toxin perfringolysin O (θ toxin, Clostridium perfringens) fused to GFP (D4-GFP)[39,40] and observation by transmission electron microscopy (TEM) showed similar levels of cholesterol staining in multivesicular bodies (MVBs) of HeLa WT and CD63 KO cells grown in the presence of serum-derived LDL-cholesterol (Extended data Fig. 5a). Treatment with U18666A, an inhibitor of the cholesterol transporter NPC1, induced similar accumulation of LDL-BODIPY associated fluorescence in endosomal compartments in both WT and CD63 KO HeLa cells, indicating that the NPC1 pathway was active in both conditions (Fig. 4a).

Next, we examined endogenous cholesterol homeostasis upon CD63 depletion by culturing cells in LPDS supplemented media. Global cellular cholesterol concentrations measured using a fluorometric method (Amplex Red) showed no significant decrease (Extended data Fig. 5b). Evaluation of changes in cholesterol homeostasis through SREBP2 cleavage state and nuclear translocation did not reveal significant differences between WT and CD63 KO cells (Extended data Fig. 5c). Imaging of Nile red positive lipid droplets also showed no change in intensity or appearance in CD63 KO cells (Extended data Fig. 5d).

Subsequently, we analyzed endogenous cholesterol by labeling cells grown in LPDS supplemented media with various dyes against cholesterol. Treatment with U18666A resulted in a relative enrichment of Filipin or D4-GFP staining in WT cells but not in CD63 KO cells (Fig. 4b,c). We identified CD63 positive structures as the subcellular localization of endogenous cholesterol by immunofluorescence using recombinant D4-GFP or expressing D4-mCherry constructs (Fig. 4d,e), and used TEM to refine cholesterol localization to ILVs of CD63 positive MVEs (Fig. 4f-h). Strikingly, CD63 KO HeLa cells showed no relative enrichment in Filipin staining upon treatment with U18666A (Fig. 4b), and the labeling with recombinant D4-GFP or D4-mCherry constructs was decreased (Fig. 4c,e,f,h). Similar defects in cholesterol sorting to ILVs were observed in MNT-1 CD63 KO and MNT-1 cells treated with CD63 siRNA (Extended data Fig. 5e,f). In WT cells we also observed MVEs completely devoid of cholesterol, supporting the existence of subpopulations of MVEs[36]. These findings suggested that CD63 generates a transient storage pool of endogenous cholesterol on ILVs that can be retrieved by the NPC1 pathway.

CD63 influences vesicular retrograde transport

In the absence of CD63, unlike other cargoes whose sorting to ILVs is compromised[18,41], cholesterol did not accumulate on the limiting membrane of MVEs (Fig. 4f-h). CD63 depletion does not affect cholesterol accumulation from lipoparticles upon U18666A treatment but from ILVs (Fig. 4a-b). Hence, the most plausible hypothesis is that in the absence of CD63,

cholesterol is retrieved from the endosomal limiting membrane before being sorted to ILVs, and is transported to other compartments. SREBP2 cleavage and nuclear translocation were unaffected by CD63 depletion (Extended data Fig. 5c), and our EM analysis excluded the mobilization of membrane contact sites in this phenotype. While cholesterol did not accumulate at the plasma membrane, we observed increased D4-GFP staining at the Golgi apparatus upon CD63 depletion in both cell types (Fig. 4g-h and Extended data Fig. 5f,g).

To further track cholesterol trafficking, we fed cells grown in LPDS supplemented media with TopFluor (TF-chol), a fluorescent analog of cholesterol that traffics like cholesterol[42,43]. TF-chol localized both at the plasma membrane and in perinuclear compartments at similar levels in WT and KO cells but displayed a more perinuclear localization in the KO condition (Fig. 5a-c). In the presence of U18666A, TF-chol intensity increased, TF-chol accumulated in swollen compartments in both conditions, but the number of TF-chol positive compartments was drastically reduced and more perinuclear in CD63 KO cells. In CD63 KO cells, the brightest compartments surrounded an area of weak diffuse fluorescent signal in the perinuclear region that may correspond to the Golgi Apparatus (Fig. 5a). Analysis of U18666A-treated cells showed increased colocalization of TF-chol with a marker of (medial-) Golgi, Mannosidase-II, and decreased colocalization with the late endosomes/lysosomes marker LAMP-1 in the absence of CD63 (Fig. 5d,e). These data suggest that cholesterol accumulates in the Golgi apparatus in the absence of CD63.

We then monitored the anterograde and retrograde transport of cargos whose trafficking is influenced by cholesterol levels[44,45]. Upon addition of biotin, viral glycoprotein VSVG inserted in the RUSH system was able to exit the ER, reach the Golgi, and the plasma membrane in both WT and CD63 KO HeLa cells, confirming that anterograde trafficking pathways are not affected by CD63 absence (Extended data Fig. 6a). Pulse chase experiments revealed an altered redistribution of cation-independent mannose 6-phosphate receptor (CI-M6PR) to the Golgi apparatus in CD63 KO HeLa cells and a similar trend in CD63 siRNA treated MNT-1 cells (Extended data Fig. 6b,c). We then focused on endogenous ApoE, a known regulator of cholesterol homeostasis expressed in MNT-1 cells but not in HeLa cells. In line with the reported role of CD63 in sorting endogenous ApoE to ILVs[20], we confirmed that siRNA-mediated depletion of CD63 or CD63 KO led to the accumulation of ApoE in TGN and Golgi and its depletion from LAMP-1 positive lysosomes (Extended data Fig. 6d-f). These data suggest that retrograde but not anterograde transport of cargos sensitive to cholesterol levels is affected in the absence of CD63.

We refined our morphological analysis of MVEs in HeLa and MNT-1 cells via TEM. In CD63 KO cells, MVEs exhibited increased tubules and budded structures nearby (Fig. 5f). EM analysis after high-pressure freezing of CD63 KO MNT-1 cells also revealed similar tubules and budded structures near endosomes corresponding to early melanosomes[18] (Extended data Fig. 7a) (positive for D4-GFP in WT cells). Given the crucial role of actin bundling in endosomal tubular domain fission for cargo recycling[3], we investigated endosome-associated actin distribution using phalloidin staining and SR-IFM. CD63 depletion led to actin accumulation around Lamp-1 positive late endosomes and EEA1 positive early endosomes, which was reversed by CK666, an Arp 2/3 complex inhibitor. Similar actin accumulation was observed in CD63 siRNA treated MNT-1 cells (Fig. 5g and Extended data Fig. 7b,c). Consistent with Arp2/3-dependent actin bundling's role in endosomal tubule fission[47], TEM analysis of CK666-treated cells showed increased endosomal tubulations in CD63 KO cells (Extended Data Fig. 7d). We then examined whether CK666 affected cholesterol trafficking, revealing altered TF-chol distribution patterns in CD63 KO cells compared to WT cells upon CK666 treatment, along with D4-GFP staining accumulation on endosomal tubular carriers in CD63 KO cells treated with CK666 (Extended data Fig. 7e,f). These findings suggest that CD63 depletion stimulates a retrograde vesicular pathway from endosomes to Golgi, mediated by Arp2/3-dependent actin polymerization, impacting the retrograde transport of CI-M6PR and endogenous ApoE differently.

CD63 accommodates cholesterol in an intramembrane cavity

A recent study identifying a cholesterol binding pocket in CD81's crystal structure[34] prompted us to construct a 3D model of CD63 WT. The model resembles the secondary topology of CD81, featuring a cone-like structure and an intramembrane cavity (Fig. 6a). Alignment of CD63 sequences with CD81 and CD9 revealed a glutamate residue at position 217 (E217) in CD63's fourth transmembrane domain (Fig. 6b), analogous to E219 in CD81, known for hydrogen bonding to cholesterol hydroxyl groups. Substituting glutamate with glutamine (E217Q) in CD63 was hypothesized to abolish cholesterol binding. We used HADDOCK to model cholesterol interaction with CD63's fourth transmembrane domain. The resulting models showed cholesterol accommodation in the intramembrane cavity of CD63 WT, whereas in CD63 E217Q, cholesterol preferred the cytoplasmic leaflet outside the cavity (Fig. 6c). Expressing WT and E217Q mutant in CD63 KO cells (Fig. 6d) demonstrated correct sorting to sEVs and ILVs (Fig. 6d,e). Filipin staining of LPDS-grown cells showed significant cholesterol accumulation with CD63 WT or E217Q, unaffected by U18666A (Fig. 6f). However, D4-GFP

and D4-mCherry staining revealed reduced cholesterol levels in CD63 E217Q upon U18666A treatment compared to CD63 WT (Fig. 6g,h and Extended Data Fig. 8a). These findings confirm CD63's role in cholesterol endosomal trafficking, associated with its ability to accommodate cholesterol in an intramembrane cavity.

CD63 regulates cholesterol trafficking to sEVs of endosomal origin

Impaired cholesterol sorting on ILVs of CD63 KO cells prompted us to investigate its relevance for ILVs secreted as exosomes. Initially, we quantified global cholesterol content in sEVs using Amplex Red assay. Cholesterol levels varied considerably in WT cells and tended to decrease in CD63 KO, though not significantly (Extended Data Fig. 8b). To refine this, we performed single vesicle analysis using EM immunogold labeling of cholesterol with D4-GFP. The labeling clustered, possibly representing cholesterol-enriched microdomains, consistent with lipid rafts[48] and tetraspanin microdomains[49] on vesicle surfaces (Fig. 7a,c, white arrowheads). sEVs from both HeLa and MNT1 cells grown in LPDS showed reduced D4-GFP labeling upon CD63 KO (average 2.6 PAG/vesicles for WT vs. 1.4 PAG/vesicles for CD63 KO for HeLa sEVs). Notably, the fraction of sEVs with low cholesterol staining (0-1 PAG/vesicles) doubled for CD63 KO EVs, while the fraction with high cholesterol staining (>4 PAG/vesicle) decreased (Extended Data Fig. 8c,d). Re-expressing CD63 WT or CD63 E217Q in HeLa CD63 KO confirmed CD63's role in cholesterol sorting to sEVs (Fig. 6d, e). Though sEV numbers remained unchanged (Extended Data Fig. 8e), D4-GFP staining on sEVs was rescued with CD63 WT but not CD63 E217Q (Fig. 7a,b). This aligned with reduced D4-GFP labeling on ILVs from CD63 E217Q-rescued cells compared to CD63 WT-rescued cells (Extended Data Fig. 8f).

The discrepancy between Amplex Red assay and other dyes can be attributed to factors such as sEV subpopulation heterogeneity, D4 and Filipin sensitivity to cholesterol esterification[50], their detection threshold at 30 mol% revealing only cholesterol-rich microdomains[51,52], the detection of GM1 by Filipin[53]. Treating cells with Bafilomycin-A1 enriched sEVs of endosomal origin (Extended Data Fig. 8g), revealing a significant decrease in cholesterol content in sEVs from CD63 KO cells (Fig. 7d). Samples not treated with esterase yielded similar results (Fig. 7d), excluding a role for CD63 in cholesteryl ester sorting.

CD63 influences the biophysical properties of sEVs

Changes of the lipid content, particularly cholesterol, of membrane leaflets influences their physical properties. To quantitatively assess the impact of cholesterol depletion on the

mechanical properties of ILVs and corresponding sEVs, we employed atomic force microscopy (AFM) nanoindentation. Overview images were obtained with imaging forces <100 pN to determine particle size distribution (Fig. 8e) Upon substrate adhesion, the flexibility of sEVs caused them to deform into various shapes, including spherical caps (Fig. 8f). Determination of the radius of curvature (Rc) of adhered sEVs by cross-sectional analysis revealed that the calculated radius (R0) of particles in solution was similar between CD63 WT and KO sEVs (Fig. 8g), consistent with NTA analysis (Fig. 1c). Indenting the center of the sEVs with the AFM tip enabled measurement of vesicle membrane stiffness (k) and determination of membrane tension and tether forces (Fig. 8h). Stiffness of HeLa WT sEVs (0.010 ± 0.002 N/m) and HeLa CD63 KO sEVs (0.010 ± 0.001 N/m) showed no significant difference. However, fitting this data to a Canham-Helfrich-theory based model to derive the bending modulus, an intrinsic membrane property, yielded 11 ± 3 kBT for HeLa WT sEVs and 14 ± 4 kBT for HeLa CD63 KO sEVs, with a statistically significant difference ($p = 0.05$). (Fig. 8i).

Cholesterol, known as a cryoprotectant, could influence sEV storage. We examined the effect of sEV storage at -80 °C on the bending modulus. Addition of data from frozen samples did not significantly alter the bending modulus of HeLa WT sEVs (12 ± 4 kBT (S.E.M., N=49)). Conversely, for HeLa CD63 KO sEVs, the bending modulus significantly increased to (19 ± 5 kBT (S.E.M., N=39), $p = 0.05$) with the addition of frozen data, indicating a direct impact of CD63 absence on sEV mechanical characteristics potentially exacerbated by specific storage conditions.

These findings suggest that CD63 KO may mechanically affect sEV membrane stiffness, correlating with cholesterol depletion.

CD63 sEVs facilitate cholesterol transfer to recipient cells

The lipid composition and biophysical properties of sEVs are believed to influence their ability to interact with and be internalized by recipient cells. To assess uptake by recipient HeLa cells, we employed a dual tagging approach to load sEVs with TF-chol and/or label them with the membrane dye MemBright[60] (Extended Data Fig. 9a), which were then fed to unlabeled cells.

Initially, we quantified absolute uptake levels by monitoring the accumulation of MemBright-associated sEVs (Fig. 8a,b). Recipient HeLa WT or CD63 KO cells exhibited similar efficiency in capturing sEVs from both HeLa WT and CD63 KO cells. As recipient cell interaction remained unaffected, we investigated whether sEVs could supply cholesterol to recipient cells akin to lipoproteins. Co-tracking of TF-chol and MemBright revealed that both tags accumulated in the same compartments within WT or CD63 KO recipient cells (Fig. 8b).

Subsequent treatment with the NPC1 inhibitor U18666A led to TF-chol accumulation in endosomal compartments of LPDS-grown recipient cells, regardless of CD63 status (Fig. 8b,c), indicating that sEVs can provide cholesterol to recipient cells through the action of NPC1/2 in host endolysosomes.

Consistent with CD63's role in cholesterol enrichment on sEVs, feeding WT or CD63 KO recipient cells with equivalent CD63 KO sEVs resulted in decreased cholesterol accumulation (Fig. 8c) but not MemBright (Fig. 8a and Extended Data Fig. 9b) compared to WT sEVs. This cholesterol supply deficiency was exacerbated following U18666A treatment (Fig. 8c). Under these conditions, minimal cholesterol accumulated in WT or CD63 KO cells when fed CD63 KO-derived sEVs (Fig. 8c and Extended Data Fig. 9c). These findings suggest that CD63 depletion and cholesterol removal from EVs do not impede their uptake by recipient cells but impair their ability to act as an external cholesterol source.

Discussion

The work identifies CD63 as a pivotal regulator of cholesterol sorting to ILVs and extracellular vesicles across different cell types. In the absence of CD63, impaired cholesterol sorting is compensated by its retrieval from endosomes via an actin-dependent vesicular pathway. Although CD63 and cholesterol depletion do not profoundly affect sEV composition or secretion, they modulate their physical characteristics. Importantly, the cholesterol sorted to ILVs forms a transient storage pool retrievable by the NPC1/2 machinery either from their origin compartment or upon ILV secretion as exosomes within recipient cell endolysosomes.

This study establishes CD63-dependent cholesterol sorting as the primary mechanism supporting the active enrichment of a lipid to ILVs and consequently to EVs likely corresponding to exosomes. Only a few lipids, including SM, FC, and CE, are enriched in EVs compared to whole cells, indicating their active sorting on ILVs or plasma membrane-derived buds. CD63 depletion or mutation uniquely impacts free cholesterol concentration, as observed through various approaches in both cell types. Other lipids like BMP are enriched on ILVs via an Alix-dependent mechanism[61] but are poorly present on EVs, suggesting that BMP-enriched ILVs are unlikely to be secreted. This supports the hypothesis that cholesterol-enriched MVE subpopulations[36,62], but not BMP-enriched ones, are preferentially secreted.

Tetraspanins, including CD63, organize as dynamic nanoclusters in membranes. While early studies highlighted the role of lipids in tetraspanin-enriched microdomain organization[9,10], it is increasingly clear that tetraspanins can also influence specific lipid presence in membranes, notably cholesterol and oxysterol. This influence may occur through tetraspanin

palmitoylation[9] or cholesterol recognition/interaction amino-acid consensus (CRAC) sequences, present in most human tetraspanins including CD63[35]. Alternatively, cholesterol could be accommodated in an intramembrane cavity formed by the four transmembrane domains, as observed for the tetraspanin CD81[34,63]. Our data suggest that this mechanism also applies to CD63, contributing to cholesterol sorting into EVs. However, the sensitivity and limitations of the various cholesterol probes used did not allowed the determination of the precise mechanism by which CD63 manages cholesterol within the membrane. We cannot discern whether CD63's role involves cholesterol translocation from the inner to the outer leaflet of the membrane bilayer or cholesterol clustering in membrane microdomains, as both processes are likely interdependent. We propose then that CD63 generates microdomains enriched in cholesterol at endosome delimiting membranes that undergo inward budding to generate cholesterol enriched ILVs. It remains uncertain whether a similar mechanism extends to other tetraspanins reported to regulate cholesterol and oxysterols, such as CD81, CD82, and TSPAN6[34,35,63, 64].

This clustering step may contribute to initial membrane bending to generate a subpopulation of ILVs[18,65] but may require additional machinery. The syntenin-alix pathway represents a potential candidate, considering CD63's direct interaction with syntenin[66] and its promotion of ESCRT-independent sorting[18] at the expense of ESCRT-I-dependent sorting[5,19,65] and the role of syntenin in CD63 sorting to ILVs[5,67]. As CD63 transiently traffics through the plasma membrane, we cannot exclude that, there, it could act on subdomains that would bud as ectosomes. Yet its primary action at MVEs is supported by its major localization in intracellular compartments[68] and its effect on cholesterol levels predominantly in intracellular compartments.

Our data strongly suggests that ILVs provide a temporary storage site for cholesterol that can be retrieved by NPC1 pathway. The increased expression of CD63 in NPC1-/- microglia would suggest that both mechanisms are tightly intricate[70]. The release of these ILVs as EVs further support the role of exosomes in clearing excess cholesterol during pathological conditions[69]. While they may represent a subset of sEVs[28], we show here that they have the capacity to deliver cholesterol to recipient cells via the NPC1/2 machinery of recipient lysosomes. This function expands the ways in which EVs function as intercellular shuttles and underscores the emerging role of EVs as trophic support[67]. The importance of this alternative cholesterol source under normal conditions is unclear. However, it could be crucial during starvation, aligning with CD63's role in autophagy[71] and likely influencing NPC1-dependent mTORC1 activity[72] or in the context of cancer, where part of the tumor might not be reached by the blood circulation.

In the absence of CD63, cholesterol is depleted from MVEs and accumulates in the Golgi. While CD63 depletion does not affect the anterograde transport of VSVG[73], our data reveal that cholesterol exits endosomes via tubular/vesicular carriers dependent on actin polymerization for their fission. The mechanism behind endosomal tubulation remains unclear but may be linked to impaired retromer function in NPC null cells[74]. This retrograde transport pathway could serve as a rescue mechanism to prevent cholesterol accumulation in endosomes, highlighting the role of retrograde transport in endosomal cholesterol homeostasis[75]. Unexpectedly, we observed delayed retrograde trafficking of CI-M6PR in CD63 KO cells, suggesting that the observed retrograde transport of cholesterol and associated proteins occurs at the expense of the conventional pathway. Normal levels of free cholesterol are required for CI-M6PR egress from endosomes[45], suggesting that altered cholesterol levels in the absence of CD63 may affect actin bundling and impair CI-M6PR's ability to recruit the retromer complex[74,76]. These findings suggest that CD63 primarily acts at the limiting membrane of MVEs, regulating cholesterol availability and lipid microdomain generation[43] to balance inward and outward budding within the endosomal pathway[2].

Previous studies have suggested diverse, cell-type-specific functions of CD63[17,18,20,22], which seem contradictory to its ubiquitous presence in MVEs and EV subpopulations across various cell types. Our current findings on CD63's fundamental role in regulating cholesterol homeostasis shed new light on these discrepancies, as several CD63-dependent cargo trafficking processes are linked to cholesterol. For instance, MHC-II, whose exosomal secretion is modulated by CD63[77], contains a cholesterol binding domain[78] while CD63-dependent sorting of ApoE[20] likely relies on ApoE's ability to associate with cholesterol, as seen during HDL formation[79]. Notably, ApoE is not expressed in HeLa cells, ruling out its involvement in CD63-dependent cholesterol trafficking. Additionally, CD63-dependent clustering of P-selectin at the plasma membrane[17] relies on cholesterol and lipid rafts, and other CD63 partners, such as Synaptotagmin VII and LMP1, contain palmitate moieties[81,82] that interact with cholesterol, potentially stabilizing their localization in CD63 and cholesterol-enriched domains. We also identified cargoes whose expression or trafficking are dependent on cholesterol (MMP12[83], BASP1[84]). It is therefore tempting to propose that the diverse roles of CD63 in distinct cell types could be supported by a central role in the regulation of cholesterol trafficking although other cargoes, such as CXCR4, may only rely on their pairing with CD63 to be targeted to endosomes in a syntenin-dependent manner[85,86]. Whether the CD63-cholesterol affects only the sorting of a precise set of transmembrane proteins, or their clustering within

membrane microdomains or the binding of soluble protein to the surface of EVs, remains an open question.

Further elucidation of the mechanisms discussed here may have implications for pathogenetic mechanisms associated with CD63[87] or with the interrelated functions of the retrograde pathway[88] and cholesterol in neurodegenerative diseases or with specific upregulation of CD63 in aging[25] and in cancer cells[89]. From a therapeutic perspective, understanding the functional relationship between CD63 and cholesterol could enhance the use of CD63 as an engineered molecular tool to transform EVs into therapeutic shuttles[90].

Acknowledgments

This work was founded by the Institut Curie International PhD Program (to R.P.), by the Fondation ARC pour la Recherche sur le Cancer (DOC20180507506 to R.P. and PGA1 RF20190208474 to MC.), by the Fondation pour la Recherche Médicale (AJE20160635884) (to G.vN.), by Institut national du Cancer grant (N°2019-125 PLBIO19°059), by ANR (ANR-20-CE18-0026-01 to G.v.N, and ANR-18-CE13-0017-02 to E.R.), by “Région Ile-de-France” and Fondation pour la Recherche Médicale grants (to D.L.), by the STW Cancer-ID program (project 14192 to WHR).

We thank the Cell and Tissue Imaging core facility (PICT IBiSA) and Nikon Imaging Centre at Institut Curie-CNRS, member of the French National Research Infrastructure France-BioImaging (ANR10-INBS-04); the NeurImag core Facility team for their technical and scientific support. NeurImag is part of IPNP, Inserm U1266 and Université Paris Cité and member of the national infrastructure France-BioImaging supported by the French National Research Agency (ANR-10-INBS-04). We also thank Leducq establishment for funding the Leica SP8 Confocal/STED 3DX system, Bettencourt foundation for funding the Leica/Yokogawa Spinning disc system, Alexis Canette and Michaël Trichet at the "Service de Microscopie Électronique (SME) de l’Institut de Biologie Paris-Seine", and Catherine Durieu at ImagoSeine core facility of Institut Jacques Monod, member of France-BioImaging (ANR-10-INBS-04) and IBiSA, with the support of Labex "Who Am I", Inserm Plan Cancer, Region Ile-de-France and Fondation Bettencourt Schueller. We thank the “Structure and Membrane Compartment” laboratory and the “Endosomal dynamic in neuropathies” laboratory for insightful discussions. We warmly thank Fabien Alpy for insightful discussions and providing essential reagents.

Author Contributions

These authors contributed equally: Roberta Palmulli and Mickaël Couty.

R.P., M.C. and G.vN. designed, performed, and analyzed most of the experiments. R.P. and G.vN. wrote the manuscript with help from M.C., M.C.P. and W.H.R.

M.C.P., S.S. and W.H.R. performed and analyzed atomic force microscopy. F.D. and D.L. performed and analyzed proteome mass spectrometry. M.P., M.L. and A.K. performed lipidomic analysis and/or analyzed lipidomic data. F.V., S.C., M.T. and E.R. performed experiments and/or generated tools/cell lines. G.R. and G.vN. acquired fundings. G.vN. conceived and supervised the study. All authors read and approved the manuscript.

Corresponding author

Correspondence to Guillaume van Niel.

Competing interests

The authors declare no competing interests.

Figure legends

Figure 1. Characterization of WT and CD63 KO HeLa and MNT-1 cells and sEVs.

a. Western blot analysis of cell lysates derived from WT or CD63 KO HeLa or MNT-1 cells. Quantification of protein content normalized to HeLa (n= 3 independent experiments, 2way ANOVA, **** P<0.0001) or MNT-1 WT (n= 3 independent experiments, multiple unpaired t-test, Holm-Šídák method, **** P< 0.0001). **b.** Western blot analysis of sEVs derived from WT or CD63 KO HeLa or MNT-1 cells and isolated by UC. Quantification of protein content normalized to HeLa (n= 3 independent experiments, 2way ANOVA, *** P= 0.0002 and ***P= 0.0003) or MNT-1 WT (n= 3 independent experiments, multiple unpaired t-test, Holm-Šídák method, * P=0.006349, **** P<0.0001). **c.** NTA analysis of sEVs derived from WT or CD63 KO HeLa cells and isolated by UC. Average number of particles/ml (n= 3 independent experiments, RM one-way ANOVA, ns P> 0.05) or size distribution (n= 3 independent experiments, 2way ANOVA, only significant results are shown, * P= 0.0465, *** P= 0.0005). **d.** NTA analysis of sEVs derived from MNT-1 cells WT or CD63 KO and isolated by SEC. Average number of particles/ml (n= 6 independent experiments, two-tailed unpaired t test, ns P= 0.9987) or size distribution (6 independent experiments, multiple unpaired Student's t test, only significant results are shown). **e.** IFM of HeLa cells WT or CD63 KO stained for LAMP-1. Bars=10 µm. Representative of 3 independent experiments. **f.** Electron micrograph of HeLa cells WT or CD63 KO. Bars=200 nm. Representative of 2 independent experiments.

Data are presented as mean values +/- SEM. Source numerical data and unprocessed blots are available in source data.

Figure 2. Proteome analysis of WT and CD63 KO HeLa and MNT-1 cells and sEVs.

a. Correlation plot of Hela WT and MNT-1 WT cell proteomes expressed as fold changes of peptide abundance (n= 5 independent experiments for cell lysates). **b.** List of proteins enriched in WT cell proteomes and common between HeLa and MNT-1. **c.** Correlation plot of Hela WT and MNT-1 WT sEV proteomes expressed as the fold changes of peptide abundance (n= 5 independent experiments for sEVs). **d.** List of proteins enriched in WT sEV proteomes and common between HeLa and MNT-1. List of Molecular function GO Terms common between HeLa WT and MNT-1 WT sEVs.

A linear model (adjusted on peptides and biological replicates) was performed, and a two sided t-test was applied on the fold change estimated by the model. The p-values were then adjusted

using the Benjamini–Hochberg FDR procedure. Source numerical data are available in source data.

Figure 3. Lipidome analysis of WT and CD63 KO HeLa and MNT-1 cells and sEVs.

a. Comparison of lipid class levels (expressed as mol% of total lipids) identified in WT HeLa cells or sEVs (n= 3 independent experiments for cell lysates and 4 independent experiments for sEVs, two-tailed Student's t test). **b.** Comparison of lipid class levels (mol% of total lipids) identified in WT MNT-1 cells or sEVs (n= 3 independent experiments for cell lysates and 5 independent experiments for sEVs, two-tailed Student's t test). **c.** Comparison of lipid class levels (mol% of total lipids) identified in WT or CD63 KO HeLa cells (n= 3 independent experiments for WT cells and 7 independent experiments for KO cells, two-tailed Student's t test). **d.** Comparison of lipid class levels (mol% of total lipids) identified in WT or CD63 KO MNT-1 cells (n= 3 independent experiments for WT cells and 3 independent experiments for KO cells, two-tailed Student's t test). **e.** Comparison of lipid class levels (mol% of total lipids) identified in sEVs derived from WT or CD63 KO HeLa cells (n= 4 independent experiments for WT sEVs and 8 independent experiments for KO sEVs, two-tailed Student's t test). **f.** Comparison of lipid class levels (mol% of total lipids) identified in sEVs derived from MNT-1 cells WT or CD63 KO (n= 5 independent experiments for WT sEVs and 5 independent experiments for KO sEVs two-tailed Student's t test). *P* value: **P*=<0.05, ***P* =<0.01, ****P* =<0.001. Data are presented as mean values +/- SEM. Source numerical data are available in source data.

List of lipids: Phosphatidylcholine (PC), Phosphatidylethanolamine (PE), Phosphatidylinositol (PI), Plasmalogen PE (PE-P), Phosphatidylserine (PS), Phosphatidylglycerol (PG), Phosphatidic acid (PA), Bis(monoacylglycero)phosphate (BMP), Lysophosphatidylcholine (LPC), Lysophosphatidylethanolamine (LPE), Lysophosphatidylglycerol (LPG), Sphingomyelin (SM), Ceramide (Cer), Dihydroceramide (DHC), Cholesterol (FC), Cholesteryl esters (CE).

Figure 4. Cholesterol localization in WT and CD63 KO HeLa cells.

a. Localization of LDL-BODIPY in WT and CD63 KO HeLa cells treated with vehicle or U18666A. Bars=10 µm. Quantification of LDL-BODIPY fluorescence intensity (n= 15 cells pooled across 1 independent experiment, Kruskal-Wallis test, *** P= 0.0006, **** P< 0.0001). **b.** Localization of cholesterol stained with filipin in WT or CD63 KO HeLa cells treated with vehicle or U18666A. Bars=10 µm. Quantification of filipin fluorescence intensity in HeLa cells

treated with U18666A, expressed as relative enrichment compared to vehicle-treated cells (n= 18 cells pooled across 2 independent experiments, Kruskal-Wallis test, * P= 0.0281). **c.** Localization of cholesterol in Hela cells WT or CD63KO treated with vehicle or U18666A, permeabilized and stained with D4-GFP. Bars=10 µm. Quantification of D4-GFP fluorescence intensity expressed as integrated density of fluorescence within cells (n=9 WT cells, 7 KO cells, 21 WT + U18666A cells, 28 KO + U18666A cells pooled across 3 independent experiments, Ordinary one-way ANOVA, ns P> 0.005, * P= 0.0148 or 0.0101, ** P= 0.0048). **d.** Colocalization of cholesterol and CD63 positive compartments in Hela cells permeabilized and stained with D4-GFP and CD63. Representative of 3 independent experiments. **e.** Localization of cholesterol in WT or CD63 KO Hela cells transfected with pD4-mCherry, treated with vehicle or U18666A and stained for CD63. Bars=10 µm. Quantification of D4-mCherry fluorescence intensity in Hela cells treated with vehicle (n=30 cells pooled across 3 independent experiments, Mann-Whitney test, ** P= 0.0019) or U18666A (n=30 cells pooled across 3 independent experiments, t-test, **** P <0.0001). **f.** HeLa cells WT or CD63 KO were grown in LPDS, processed for ultrathin cryo-sectioning and immuno-gold labeled with D4-GFP (PAG 10nm) and CD63 (PAG 5nm). Bars=200 nm. MVEs containing cholesterol are shown. Bars= 200 nm. Representative of 3 independent experiments, quantified in (**h**). **g.** HeLa cells WT or CD63 KO were grown in LPDS, processed for ultrathin cryo-sectioning and immuno-gold labeled with D4-GFP (PAG 10nm). White arrows indicate MVEs containing cholesterol, black arrows indicate Golgi apparatus, and arrowheads indicate transport vesicles containing cholesterol. Bars=200 nm. Representative of 3 independent experiments, quantified in (**h**). **h.** Quantification of the number of gold particles on intraluminal vesicles (ILVs) per MVE, MVE limiting membrane (LM) and Golgi apparatus (MVEs, H WT n=92, H CD63 KO#1 n=41, H CD63 KO#2 n=115; Golgi, H WT n=18 H CD63 KO#1 n=17, H CD63 KO#2 n=34; pooled across 3 independent experiments, 2-way ANOVA multiple comparisons, ns P > 0.05, **** P< 0.0001). Data are presented as mean values +/- SEM. Source numerical data are available in source data.

Figure 5. Absence of CD63 induces accumulation of cholesterol at the Golgi apparatus and actin-dependent endosomal tubulations.

a. Localization of TF-chol in WT and CD63 KO HeLa cells treated with vehicle or U18666A. Bars=10 µm. Red circle indicates perinuclear accumulation of TF-chol. A 3D view of HeLa cells treated with U18666A is shown in the bottom panel, with white arrows indicating the perinuclear accumulation of TF-chol. Representative of 3 independent experiments quantified

in (**b**,**c**) **b.** Quantification of TF-chol fluorescence intensity in positive compartments of WT or CD63 KO Hela cells treated with vehicle or U18666A (n= 35 cells pooled across 3 independent experiments, Kruskal-Wallis test, ns P>0.9999, ** P= 0.0025, *** P= 0.0001, **** P< 0.0001). Quantification of the size (n=35 cells pooled across 3 independent experiments, Kruskal-Wallis test, ns P= 0.6459, * P= 0.0276, ** P= 0.0050, **** P<0.0001) and the number of TF-chol positive compartments in WT or CD63 KO Hela cells treated with vehicle or U18666A. (n=35 cells pooled across 3 independent experiments, Kruskal-Wallis test, ns >0.005, ** P= 0.0041, **** P<0.0001). **c.** Quantification of the localization of TF-chol positive compartments within WT or CD63 KO Hela cells treated with vehicle or U18666A. Data are expressed as percentage of compartments in the perinuclear area or in the periphery (n=25 cells pooled across 3 independent experiments, 2-way ANOVA, ns P>0.005, * P= 0.0260, ** P= 0046, *** P= 0.0005). **d-e.** Localization of TF-chol in WT and CD63 KO HeLa cells transfected with the Golgi marker Mann-II-mCherry (**d**) or with the late endosomal marker LAMP-1-mCherry (**e**) and treated with U18666A. Bars=10 µm. Manders' colocalization coefficient between TF-chol and Mann-II 1 (n=13 WT cells, n= 12 KO cells pooled across 2 independent experiments, two-tailed unpaired t-test, *** P= 0.0009) or LAMP-1 (n= 17 WT cells, 15 KO cells pooled across 2 independent experiments, two-tailed unpaired t-test, * P= 0.0104). **f.** Electron micrograph of HeLa cells WT or CD63 KO analyzed by 2D EM. Bars= 200 nm. Quantification of the number of tubules/buds per endosome (n= number of MVEs, H WT n=24, H CD63 KO#1 n=22, H CD63 KO#2 n=18; pooled across 2 independent experiments, Ordinary one-way ANOVA, ns P= 0.9033, ** P= 0.0062 and 0.0067). **g.** SR-IFM of HeLa cells WT or CD63 KO treated with DMSO or CK666 and co-stained for LAMP-1 and actin. Bars= 10 µm, bars= 5 µm for magnifications. Normalized phalloidin fluorescence on LAMP-1-positive endosomes in HeLa cells treated with DMSO or CK666 (n=number of endosomes, H WT DMSO n=816, H CD63 KO#1 DMSO n=725, H CD63 KO#2 DMSO n=974, H WT CK666 n=341, H CD63 KO#1 CK666 n=385, H CD63 KO#2 CK666 n=258; pooled across 3 independent experiments, Kruskal-Wallis test, *** P= 0.0006, **** P< 0.0001). Data are presented as mean values +/- SEM. Source numerical data are available in source data.

Figure 6. CD63 presents an intramembrane cavity able to accommodate cholesterol.

a. Modeling of CD63 WT structure generated with I-TASSER suite (C-score= 0.23) (rainbow colors), superimposed on CD81 structure (purple sharp line). **b.** Sequence alignment of CD63, CD81, and CD9. Sequences were obtained from Uniprot and alignment was performed using CLUSTAL O (1.2.4). Red square represents the glutamate residue in CD63 (E217) that was

mutated in this study. Green square represents the glutamate residue in CD81 (E219) that was mutated in CD81[34]. Blue squares indicate the regions corresponding to the transmembrane domains. **c.** Modeling of CD63 WT or E217Q interaction with a cholesterol molecule created with Haddock 2.4 suite. Magnification shows CD63 residues predicted to interact with cholesterol (yellow structure). **d.** Western blot analysis of cell lysates and sEVs from WT or CD63 KO or CD63 KO HeLa cells rescued with CD63 WT or mutant E217Q. Representative of 3 independent experiments. **e.** CD63 KO HeLa cells were grown in LPDS, rescued with CD63 WT or mutant E217Q, processed for ultrathin cryo-sectioning and immuno-gold labeled with D4-GFP (PAG 10nm) and CD63 (PAG 5nm). Bars=200 nm. Representative of 2 independent experiments. **f.** Localization of cholesterol stained with filipin in HeLa cells CD63 KO rescued with CD63 WT or CD63 E217Q and treated with vehicle or U18666A. Bars=10 µm. Quantification of filipin fluorescence intensity in HeLa cells treated with U18666A (n=18 cells pooled across 2 independent experiments, Kruskal-Wallis test, ns P> 0.9999). **g.** Localization of CD63 and recombinant D4-GFP in HeLa CD63 KO cells rescued with CD63 WT or CD63 E217Q and treated with U18666A. Bars=10 µm. Quantification of D4-GFP integrated density of fluorescence (n= 13 CD63 KO + CD63 WT cells, 9 CD63 KO + CD63 E217Q cells pooled across 2 independent experiments, two-tailed Mann-Whitney test, ** P= 0.0071). **h.** Localization of CD63 and expressed D4-mCherry in Hela cells CD63 KO cells rescued with CD63 WT or CD63 E217Q and treated with U18666A. Bars =10 µm. Quantification of D4-mCherry integrated density of fluorescence (n= 17 CD63 KO + CD63 WT cells, 21 CD63 KO + CD63 E217Q cells pooled across 3 independent experiments, two-tailed t-test, ** P= 0.0072). Data are presented as mean values +/- SEM. Source numerical data and unprocessed blots are available in source data.

Figure 7. CD63 modulates cholesterol trafficking to sEVs and exosomes, affecting their biophysical properties.

a. sEVs were isolated from HeLa cells (grown in LPDS) WT or CD63 KO or CD63 KO rescued with CD63 WT or CD63 E217Q and observed by electron microscopy after immunogold labeling with D4-GFP (PAG 10nm). Bars=200 nm. **b.** Quantification of the number of gold particles per EV (n=number of sEVs, H WT n=1201, H CD63 KO#2 n=942, pooled across 4 independent experiments, H CD63 KO#1 n=524, H CD63 KO#2+CD63 WT n=1368, H CD63 KO#2+CD63 E217Q n=1035 pooled across 2 independent experiments, Kruskal-Wallis test, ns P> 0.9999, ns P= 0.1275, * P= 0.0100, **** P< 0.0001). **c.** sEVs were isolated from MNT-1 cells WT or CD63 KO grown in LPDS and observed by electron microscopy after immunogold

labeling with D4-GFP (PAG 10nm). Bars=200 nm. Quantification of the number of gold particles per EV (n=number of sEVs, M WT n=509, M CD63 KO n=426; pooled across 2 independent experiments, two-tailed Mann-Whitney test, **** P< 0.0001). **d.** Cholesterol content of sEVs isolated from Bafilomycin-A1 treated HeLa cells (grown in LPDS) WT or CD63 KO and measured by Amplex Red assay (including or not cholesterol esterase). Cholesterol content is normalized to the number of vesicles (g of chol per single sEV). (n= 4 for WT, n=5 for KO independent experiments for condition without esterase, two-tailed Mann Whitney test, * P=0.0159; n= 7 independent experiments for condition with esterase, two-tailed unpaired t test, * P= 0.0104). **e.** AFM topography image of H WT sEVs (left) and H CD63 KO#2 sEVs (right) attached to glass coverslip coated with poly-L-lysine (PLL). Color scale indicates height. **f.** Deformation distribution of sEVs upon substrate adhesion determined by their height (H) over radius of curvature (R_c): The averaged ratio was 1.41 ± 0.06 (S.E.M., N=42 sEVs) for H WT and 1.35 ± 0.04 (S.E.M., N=45 sEVs) for H CD63 KO#2. The inset in the lower left corner illustrates reference shapes for H/R_c equals 0.5, 1, and 2. Boxplots are shown in which the center line indicates median, box limits indicate upper and lower quartiles and whiskers indicate 1.5x interquartile range. **g.** Distribution of calculated radii R_0 of the sEVs while in solution. Mean radius of the sEVs is 64 ± 4 nm (S.E.M., N=42 sEVs) for H WT sEVs and 69 ± 2 nm (S.E.M., N=45 sEVs) for H CD63 KO#2 sEVs. **h.** Stiffness of sEVs obtained by linearly fitting force indentation curves between 0.02 – 0.1 R_c. Mean values are 0.010 ± 0.002 N/m (S.E.M., N=42 sEVs) for H WT sEVs, and 0.010 ± 0.001 N/m (S.E.M., N=45 sEVs) for H CD63 KO#2 sEVs. Boxplots are shown in which the center line indicates median, box limits indicate upper and lower quartiles and whiskers indicate 1.5x interquartile range. **i.** Dimensionless pressure vs. dimensionless stiffness for sEVs. The theoretically predicted curve is displayed as solid red line. Data for H WT sEVs and H CD63 KO#2 sEVs were individually fitted to the theoretical curve with the bending modulus κ as parameter. Bending moduli obtained for H WT sEVs and H CD63 KO#2 are κ = (11 ± 3) k_BT (S.E.M, N = 36 sEVs), and κ = (14 ± 4) k_BT (S.E.M., N = 30 sEVs), respectively. The error was determined using the bias corrected percentile method with 500 bootstrapping repetitions. A two-sided t-test revealed a significant difference between the bending moduli (p = 0.05).

Data are presented as mean values +/- SEM. Source numerical data are available in source data.

Figure 8 . CD63 sEVs can transfer cholesterol to recipient cells.

a. WT or CD63 KO HeLa sEVs were labeled with MemBright-640 and incubated overnight with WT or CD63 KO HeLa cells. Bars= 10 µm. Quantification of MemBright-640 intensity in

WT and CD63 KO HeLa cells (n=10 cells pooled across 2 independent experiments, Ordinary One-way ANOVA test, ns P> 0.05, * P=0.0328). **b.** WT HeLa cells were labeled with TF-chol, sEVs containing TF-chol were isolated, labeled with MemBright-640, and incubated overnight with WT or CD63 KO HeLa cells treated with vehicle or U18666A. Bars= 10um. Quantification of Membright-640 intensity in recipient WT and CD63 KO HeLa cells treated or not with U18666A (n=10 cells pooled across 2 independent experiments, Kruskal-Wallis test, ns P > 0.9999, ns P = 0.3203, ns P= 0.5110, ns P= 0.7278). Quantification of TF- chol intensity in recipient WT and CD63 KO Hela cells treated or not with U18666A (n=12 cells pooled across 2 independent experiments, Kruskal-Wallis test, ns P=0.6785, ns P>0.9999, * P=0.05, ** P=0.0028, **** P <0.0001). **c.** WT or CD63 KO HeLa cells were labeled with TF-chol, sEVs containing TF-chol were isolated, and incubated overnight with CD63 KO HeLa cells treated with vehicle or U18666A. Bars=10 µm. Quantification of TF-chol intensity in recipient WT or CD63 KO HeLa cells. (n=9 cells pooled across 2 independent experiments, Ordinary One-way ANOVA test, * P= 0.0431, ** P= 0.0097, *** P= 0.0006, **** P< 0.0001). Data are presented as mean values +/- SEM in **a** and **b**. Data in **c** are presented as violin plot with median and quartiles. Source numerical data are available in source data.

References

1. Naslavsky, N. & Caplan, S. The enigmatic endosome – sorting the ins and outs of endocytic trafficking. *J. Cell Sci.* **131**, jcs216499 (2018).
2. Cullen, P. J. & Steinberg, F. To degrade or not to degrade: mechanisms and significance of endocytic recycling. *Nat. Rev. Mol. Cell Biol.* **19**, 679–696 (2018).
3. Simonetti, B. & Cullen, P. J. Actin-dependent endosomal receptor recycling. *Curr. Opin. Cell Biol.* **56**, 22–33 (2019).
4. Hurley, J. H. ESCRTs are everywhere. *EMBO J.* **34**, 2398–2407 (2015).
5. Baietti, M. F. *et al.* Syndecan-syntenin-ALIX regulates the biogenesis of exosomes. *Nat. Cell Biol.* **14**, 677–685 (2012).
6. van Niel, G., D'Angelo, G. & Raposo, G. Shedding light on the cell biology of extracellular vesicles. *Nat. Rev. Mol. Cell Biol.* **19**, 213–228 (2018).
7. van Niel, G. *et al.* Challenges and directions in studying cell–cell communication by extracellular vesicles. *Nat. Rev. Mol. Cell Biol.* **23**, 369–382 (2022).
8. Tekirdag, K. & Cuervo, A. M. Chaperone-mediated autophagy and endosomal microautophagy: Joint by a chaperone. *J. Biol. Chem.* **293**, 5414–5424 (2018).
9. Charrin, S. *et al.* A physical and functional link between cholesterol and tetraspanins. *Eur. J. Immunol.* **33**, 2479–2489 (2003).
10. Odintsova, E. *et al.* Gangliosides play an important role in the organization of CD82-enriched microdomains. *Biochem. J.* **400**, 315–325 (2006).
11. Charrin, S. *et al.* Lateral organization of membrane proteins: tetraspanins spin their web. *Biochem. J.* **420**, 133–154 (2009).
12. Escola, J. M. *et al.* Selective enrichment of tetraspan proteins on the internal vesicles of multivesicular endosomes and on exosomes secreted by human B-lymphocytes. *J. Biol. Chem.* **273**, 20121–20127 (1998).
13. Corso, G. *et al.* Systematic characterization of extracellular vesicle sorting domains and quantification at the single molecule – single vesicle level by fluorescence correlation spectroscopy and single particle imaging. *J. Extracell. Vesicles* **8**, 1663043 (2019).
14. Gupta, D. *et al.* Amelioration of systemic inflammation via the display of two different decoy protein receptors on extracellular vesicles. *Nat. Biomed. Eng.* **5**, 1084–1098 (2021).
15. Pols, M. S. & Klumperman, J. Trafficking and function of the tetraspanin CD63. *Exp. Cell Res.* **315**, 1584–1592 (2009).

16. Yoshida, T., Ebina, H. & Koyanagi, Y. N-linked glycan-dependent interaction of CD63 with CXCR4 at the Golgi apparatus induces downregulation of CXCR4. *Microbiol. Immunol.* **53**, 629–635 (2009).
17. Doyle, E. L. *et al.* CD63 is an essential cofactor to leukocyte recruitment by endothelial P-selectin. *Blood* **118**, 4265–4273 (2011).
18. van Niel, G. *et al.* The tetraspanin CD63 regulates ESCRT-independent and -dependent endosomal sorting during melanogenesis. *Dev. Cell* **21**, 708–721 (2011).
19. Colombo, M. *et al.* Analysis of ESCRT functions in exosome biogenesis, composition and secretion highlights the heterogeneity of extracellular vesicles. *J. Cell Sci.* **126**, 5553–5565 (2013).
20. van Niel, G. *et al.* Apolipoprotein E Regulates Amyloid Formation within Endosomes of Pigment Cells. *Cell Rep.* **13**, 43–51 (2015).
21. Hurwitz, S. N. *et al.* CD63 Regulates Epstein-Barr Virus LMP1 Exosomal Packaging, Enhancement of Vesicle Production, and Noncanonical NF-κB Signaling. *J. Virol.* **91**, (2017).
22. Verweij, F. J. *et al.* LMP1 association with CD63 in endosomes and secretion via exosomes limits constitutive NF-κB activation. *EMBO J.* **30**, 2115–2129 (2011).
23. Mathieu, M. *et al.* Specificities of exosome versus small ectosome secretion revealed by live intracellular tracking of CD63 and CD9. *Nat. Commun.* **12**, 4389 (2021).
24. Hemler, M. E. Targeting of tetraspanin proteins — potential benefits and strategies. *Nat. Rev. Drug Discov.* **7**, 747–758 (2008).
25. De Silva, N. S. *et al.* Nuclear envelope disruption triggers hallmarks of aging in lung alveolar macrophages. *Nat. Aging* **3**, 1251–1268 (2023).
26. Dooley, K. *et al.* A versatile platform for generating engineered extracellular vesicles with defined therapeutic properties. *Mol. Ther.* **29**, 1729–1743 (2021).
27. Filippini, F. *et al.* Secretion of VGF relies on the interplay between LRRK2 and post-Golgi v-SNAREs. *Cell Rep.* **42**, 112221 (2023).
28. Fordjour, F. K., Guo, C., Ai, Y., Daaboul, G. G. & Gould, S. J. A shared, stochastic pathway mediates exosome protein budding along plasma and endosome membranes. *J. Biol. Chem.* **298**, 102394 (2022).
29. Fan, Y. *et al.* Differential proteomics argues against a general role for CD9, CD81 or CD63 in the sorting of proteins into extracellular vesicles. *J. Extracell. Vesicles* **12**, 12352 (2023).
30. Skotland, T., Sagini, K., Sandvig, K. & Llorente, A. An emerging focus on lipids in extracellular vesicles. *Adv. Drug Deliv. Rev.* **159**, 308–321 (2020).

31. Subra, C., Laulagnier, K., Perret, B. & Record, M. Exosome lipidomics unravels lipid sorting at the level of multivesicular bodies. *Biochimie* **89**, 205–212 (2007).
32. Bissig, C. & Gruenberg, J. Lipid Sorting and Multivesicular Endosome Biogenesis. *Cold Spring Harb. Perspect. Biol.* **5**, a016816 (2013).
33. Trajkovic, K. *et al.* Ceramide Triggers Budding of Exosome Vesicles into Multivesicular Endosomes. *Science* **319**, 1244–1247 (2008).
34. Zimmerman, B. *et al.* Crystal Structure of a Full-Length Human Tetraspanin Reveals a Cholesterol-Binding Pocket. *Cell* **167**, 1041-1051.e11 (2016).
35. Huang, C., Hays, F. A., Tomasek, J. J., Benyajati, S. & Zhang, X. A. Tetraspanin CD82 interaction with cholesterol promotes extracellular vesicle–mediated release of ezrin to inhibit tumour cell movement. *J. Extracell. Vesicles* **9**, 1692417 (2020).
36. Möbius, W. *et al.* Recycling compartments and the internal vesicles of multivesicular bodies harbor most of the cholesterol found in the endocytic pathway. *Traffic Cph. Den.* **4**, 222–231 (2003).
37. Meng, Y., Heybrock, S., Neculai, D. & Saftig, P. Cholesterol Handling in Lysosomes and Beyond. *Trends Cell Biol.* **30**, 452–466 (2020).
38. Iaea, D. B. & Maxfield, F. R. Cholesterol trafficking and distribution. *Essays Biochem.* **57**, 43–55 (2015).
39. Shimada, Y., Maruya, M., Iwashita, S. & Ohno-Iwashita, Y. The C-terminal domain of perfringolysin O is an essential cholesterol-binding unit targeting to cholesterol-rich microdomains. *Eur. J. Biochem.* **269**, 6195–6203 (2002).
40. Wilhelm, L. P. *et al.* STARD3 mediates endoplasmic reticulum-to-endosome cholesterol transport at membrane contact sites. *EMBO J.* **36**, 1412–1433 (2017).
41. Edgar, J. R., Willén, K., Gouras, G. K. & Futter, C. E. ESCRTs regulate amyloid precursor protein sorting in multivesicular bodies and intracellular amyloid-β accumulation. *J. Cell Sci.* **128**, 2520–2528 (2015).
42. Hölttä-Vuori, M. *et al.* BODIPY-cholesterol: a new tool to visualize sterol trafficking in living cells and organisms. *Traffic Cph. Den.* **9**, 1839–1849 (2008).
43. Hölttä-Vuori, M., Sezgin, E., Eggeling, C. & Ikonen, E. Use of BODIPY-Cholesterol (TF-Chol) for Visualizing Lysosomal Cholesterol Accumulation. *Traffic Cph. Den.* **17**, 1054–1057 (2016).
44. Ying, M., Grimmer, S., Iversen, T.-G., Van Deurs, B. & Sandvig, K. Cholesterol loading induces a block in the exit of VSVG from the TGN. *Traffic Cph. Den.* **4**, 772–784 (2003).

45. Miwako, I., Yamamoto, A., Kitamura, T., Nagayama, K. & Ohashi, M. Cholesterol requirement for cation-independent mannose 6-phosphate receptor exit from multivesicular late endosomes to the Golgi. *J. Cell Sci.* **114**, 1765–1776 (2001).

46. Boncompain, G. *et al.* Synchronization of secretory protein traffic in populations of cells. *Nat. Methods* **9**, 493–498 (2012).

47. Derivery, E. *et al.* The Arp2/3 activator WASH controls the fission of endosomes through a large multiprotein complex. *Dev. Cell* **17**, 712–723 (2009).

48. Dubois, L., Ronquist, K. (K). G., Ek, B., Ronquist, G. & Larsson, A. Proteomic Profiling of Detergent Resistant Membranes (Lipid Rafts) of Prostasomes*. *Mol. Cell. Proteomics* **14**, 3015–3022 (2015).

49. McNamara, R. P. *et al.* Imaging of surface microdomains on individual extracellular vesicles in 3-D. *J. Extracell. Vesicles* **11**, e12191 (2022).

50. Savinov, S. N. & Heuck, A. P. Interaction of Cholesterol with Perfringolysin O: What Have We Learned from Functional Analysis? *Toxins* **9**, 381 (2017).

51. Sezgin, E., Levental, I., Mayor, S. & Eggeling, C. The mystery of membrane organization: composition, regulation and roles of lipid rafts. *Nat. Rev. Mol. Cell Biol.* **18**, 361–374 (2017).

52. Maekawa, M. Domain 4 (D4) of Perfringolysin O to Visualize Cholesterol in Cellular Membranes—The Update. *Sensors* **17**, 504 (2017).

53. Arthur, J. R., Heinecke, K. A. & Seyfried, T. N. Filipin recognizes both GM1 and cholesterol in GM1 gangliosidosis mouse brain. *J. Lipid Res.* **52**, 1345–1351 (2011).

54. Edgar, J. R., Manna, P. T., Nishimura, S., Banting, G. & Robinson, M. S. Tetherin is an exosomal tether. *eLife* **5**, e17180 (2016).

55. Vorselen, D., MacKintosh, F. C., Roos, W. H. & Wuite, G. J. L. Competition between Bending and Internal Pressure Governs the Mechanics of Fluid Nanovesicles. *ACS Nano* **11**, 2628–2636 (2017).

56. Vorselen, D. *et al.* The fluid membrane determines mechanics of erythrocyte extracellular vesicles and is softened in hereditary spherocytosis. *Nat. Commun.* **9**, 4960 (2018).

57. Sorkin, R. *et al.* Nanomechanics of Extracellular Vesicles Reveals Vesiculation Pathways. *Small* **14**, 1801650 (2018).

58. Sorkin, R. *et al.* Synaptotagmin-1 and Doc2b Exhibit Distinct Membrane-Remodeling Mechanisms. *Biophys. J.* **118**, 643–656 (2020).

59. Lee, D.-K., Kwon, B. S. & Ramamoorthy, A. Freezing Point Depression of Water in Phospholipid Membranes: A Solid-State NMR Study. *Langmuir* **24**, 13598–13604 (2008).

60. Collot, M. *et al.* MemBright: A Family of Fluorescent Membrane Probes for Advanced Cellular Imaging and Neuroscience. *Cell Chem. Biol.* **26**, 600-614.e7 (2019).
61. Matsuo, H. *et al.* Role of LBPA and Alix in Multivesicular Liposome Formation and Endosome Organization. *Science* **303**, 531–534 (2004).
62. Möbius, W. *et al.* Immunoelectron microscopic localization of cholesterol using biotinylated and non-cytolytic perfringolysin O. *J. Histochem. Cytochem. Off. J. Histochem. Soc.* **50**, 43–55 (2002).
63. Palor, M. *et al.* Cholesterol sensing by CD81 is important for hepatitis C virus entry. *J. Biol. Chem.* **295**, 16931–16948 (2020).
64. Molostvov, G. *et al.* Tspan6 stimulates the chemoattractive potential of breast cancer cells for B cells in an EV- and LXR-dependent manner. *Cell Rep.* **42**, 112207 (2023).
65. Edgar, J. R., Eden, E. R. & Futter, C. E. Hrs- and CD63-dependent competing mechanisms make different sized endosomal intraluminal vesicles. *Traffic Cph. Den.* **15**, 197–211 (2014).
66. Latysheva, N. *et al.* Syntenin-1 is a new component of tetraspanin-enriched microdomains: mechanisms and consequences of the interaction of syntenin-1 with CD63. *Mol. Cell. Biol.* **26**, 7707–7718 (2006).
67. Verweij, F. J. *et al.* Live Tracking of Inter-organ Communication by Endogenous Exosomes In Vivo. *Dev. Cell* **48**, 573-589.e4 (2019).
68. Edgar, J. R., Manna, P. T., Nishimura, S., Banting, G. & Robinson, M. S. Tetherin is an exosomal tether. *eLife* **5**, (2016).
69. Strauss, K. *et al.* Exosome secretion ameliorates lysosomal storage of cholesterol in Niemann-Pick type C disease. *J. Biol. Chem.* **285**, 26279–26288 (2010).
70. Colombo, A. *et al.* Loss of NPC1 enhances phagocytic uptake and impairs lipid trafficking in microglia. *Nat. Commun.* **12**, 1158 (2021).
71. Hurwitz, S. N., Cheerathodi, M. R., Nkosi, D., York, S. B. & Meckes, D. G. Tetraspanin CD63 Bridges Autophagic and Endosomal Processes To Regulate Exosomal Secretion and Intracellular Signaling of Epstein-Barr Virus LMP1. *J. Virol.* **92**, e01969-17 (2018).
72. Castellano, B. M. *et al.* Lysosomal cholesterol activates mTORC1 via an SLC38A9–Niemann-Pick C1 signaling complex. *Science* **355**, 1306–1311 (2017).
73. Lippincott-Schwartz, J. & Phair, R. D. Lipids and Cholesterol as Regulators of Traffic in the Endomembrane System. *Annu. Rev. Biophys.* **39**, 559–578 (2010).
74. Dominko, K. *et al.* Impaired Retromer Function in Niemann-Pick Type C Disease Is Dependent on Intracellular Cholesterol Accumulation. *Int. J. Mol. Sci.* **22**, 13256 (2021).

75. Marquer, C. *et al.* Arf6 controls retromer traffic and intracellular cholesterol distribution via a phosphoinositide-based mechanism. *Nat. Commun.* **7**, 11919 (2016).
76. Bucki, R. *et al.* Lateral distribution of phosphatidylinositol 4,5-bisphosphate in membranes regulates formin- and ARP2/3-mediated actin nucleation. *J. Biol. Chem.* **294**, 4704–4722 (2019).
77. Petersen, S. H. *et al.* The role of tetraspanin CD63 in antigen presentation via MHC class II. *Eur. J. Immunol.* **41**, 2556–2561 (2011).
78. Roy, K., Ghosh, M., Pal, T. K., Chakrabarti, S. & Roy, S. Cholesterol lowering drug may influence cellular immune response by altering MHC II function. *J. Lipid Res.* **54**, 3106–3115 (2013).
79. Horiuchi, Y. *et al.* Characterization of the cholesterol efflux of apolipoprotein E-containing high-density lipoprotein in THP-1 cells. *Biol. Chem.* **400**, 209–218 (2019).
80. Setiadi, H. & McEver, R. P. Clustering endothelial E-selectin in clathrin-coated pits and lipid rafts enhances leukocyte adhesion under flow. *Blood* **111**, 1989–1998 (2008).
81. Verweij, F. J. *et al.* Exosomal sorting of the viral oncoprotein LMP1 is restrained by TRAF2 association at signalling endosomes. *J. Extracell. Vesicles* **4**, 26334 (2015).
82. Flannery, A. R., Czibener, C. & Andrews, N. W. Palmitoylation-dependent association with CD63 targets the Ca2+ sensor synaptotagmin VII to lysosomes. *J. Cell Biol.* **191**, 599–613 (2010).
83. Liao, G. *et al.* Enhanced expression of matrix metalloproteinase-12 contributes to Npc1 deficiency-induced axonal degeneration. *Exp. Neurol.* **269**, 67–74 (2015).
84. Loats, A. E. *et al.* Cholesterol is required for transcriptional repression by BASP1. *Proc. Natl. Acad. Sci.* **118**, e2101671118 (2021).
85. Yoshida, T. *et al.* A CD63 Mutant Inhibits T-cell Tropic Human Immunodeficiency Virus Type 1 Entry by Disrupting CXCR4 Trafficking to the Plasma Membrane. *Traffic* **9**, 540–558 (2008).
86. Gordón-Alonso, M. *et al.* The PDZ-adaptor protein syntenin-1 regulates HIV-1 entry. *Mol. Biol. Cell* **23**, 2253–2263 (2012).
87. D'Acunzo, P. *et al.* Enhanced generation of intraluminal vesicles in neuronal late endosomes in the brain of a Down syndrome mouse model with endosomal dysfunction. *Dev. Neurobiol.* **79**, 656–663 (2019).
88. Williams, E. T., Chen, X., Otero, P. A. & Moore, D. J. Understanding the contributions of VPS35 and the retromer in neurodegenerative disease. *Neurobiol. Dis.* **170**, 105768 (2022).

89. Kaprio, T., Hagström, J., Andersson, L. C. & Haglund, C. Tetraspanin CD63 independently predicts poor prognosis in colorectal cancer. *Histol. Histopathol.* **35**, 887–892 (2020).
90. Gupta, D. *et al.* Quantification of extracellular vesicles in vitro and in vivo using sensitive bioluminescence imaging. *J. Extracell. Vesicles* **9**, 1800222 (2020).

Methods

Cell culture, transfection, and drug treatments

HeLa Kyoto were originally obtained from ATCC and gifted to us by Dr. Bruno Goud's laboratory (CNRS UMR144, Institut Curie, Paris, France). MNT-1 cells were originally obtained from ATCC and gifted to us by Dr. Michael S. Marks (Children's Hospital of Philadelphia, Philadelphia, USA). HeLa cells were cultured in DMEM Glutamax (Gibco) supplemented with 10% (v/v) FBS, 1% penicillin-streptomycin (Gibco). MNT-1 cells were cultured in DMEM Glutamax (Gibco) supplemented with 20% FBS, 10% AIM-V medium, sodium pyruvate, nonessential amino acids, and penicillin-streptomycin (Gibco). Where indicated, FBS was substituted by LPDS 1/30 (Millipore Merck). All cells were maintained at 37°C in a 5% (v/v) CO_2 incubator. For siRNA transfection, MNT-1 cells were seeded at day 1, transfected with siRNAs (200 pmol) at day 3 and at day 5 using Oligofectamine (Thermo Fisher Scientific), according to the manufacturer's instructions, and analyzed at day 7. For rescue experiments, HeLa cells were microporated using the Neon Electroporation Transfection System (Invitrogen, Thermo Fisher Scientific) with 0.5 ug of plasmid according to the manufacturer`s protocol using the following settings: two pulses at 1.005 V with 35-ms pulse width. For plasmid transfection, cells were transfected using JetPrime Transfection reagent (Polyplus-Transfection) according to the manufacturer's protocol.

CK666 (Tocris Biosciences) treatments were for 2 h at 200 µM. U18666A (Sigma Aldrich chimie) treatments were for 16h at 1 µM. Bafilomycin-A1 (Sigma Aldrich chimie) treatments were for 2 h at 100 nM.

Generation of CRISPR/CAS9 CD63 KO

CD63 KO HeLa or MNT-1 cells were generated using CRISPR/Cas9 gene editing technology. The target sequence (CCAGTGGTCATCATCGCAGT) was selected using the CRISPR design tool available at the Broad Institute (https://portals.broadinstitute.org/gpp/public/analysis-tools/sgrna-design). The corresponding guide DNA sequences were cloned into the lentiCRISPRv2 plasmid (Addgene#52961) according to the instructions of the Zhang laboratory (http://www.genome-engineering.org/gecko/)[91]. The plasmid was transfected using FuGENE HD according to the manufacturer's instructions for HeLa cells, and the Neon Electroporation Transfection System (Invitrogen, Thermo Fisher Scientific) for MNT-1 cells. MNT-1 cells were microporated with 0.5 ug of plasmid following optimized settings: three pulses at 1.400 V with 10-ms pulse width. After 36-48h, cells were treated with 10 µg/ml

puromycin for 48h. Cells negative for CD63 were sorted following staining with the CD63 mAb TS63 using a FACS Aria cell sorter (Beckton Dickinson). CD63 KO HeLa clones #1 and #2 were obtained by single-cell culture in 96-well plates.

Reagents, antibodies, plasmids, and siRNAs

Reagents were obtained from the following sources: recombinant D4-GFP was a kind gift of Fabien Alpy (IGBMC, Illkirch, France), phalloidin conjugated to Alexa Fluor 647, LDL-Bodipy, and Nile Red from Thermo Fisher Scientific, (810255P) and Filipin III (F4767) from Sigma Aldrich chimie.

Antibodies were obtained from the following sources: anti-CD63 (CLB-180, Thermo Fisher Scientific, or ab23792, Abcam, 1:200 for WB, IF and EM), anti-CD9 (mAb TS9) and anti-CD63 (mAb TS63) were a kind gift of Eric Rubinstein (CIMI, Paris, France), anti-alix (pab0204, Covalab, 1:500 for WB), anti- syntenin (ab19903, Abcam, 1:500 for WB), anti-tubulin (ab6046, Abcam, 1:10,000 for WB), anti-ß-actin (A5316, Sigma, 1:2000 for WB), anti-ApoE (ab52607, Abcam, 1:500 for IF and WB), anti-EEA1 (ab70521, Abcam, 1:200 for IF), anti-TGN46 (AHP500GT, Biorad, 1:300 for IF), anti-GM130 (610822, BD Transduction Laboratories, 1:1000 for IF), anti-CI-M6PR (ab8093, Abcam, 1:100 for pulse/chase), anti-LAMP-1 (555798, BD Biosciences, 1:200 for IF), anti-GFP (A11122, Thermo Fisher Scientific, 1:400 for EM), anti-SREBP2 (Clone # 751512, MAB7119, R&D Systems, 1:250 for WB).

Secondary anti-rabbit IgG or anti- mouse IgG anti-sheep IgG antibodies conjugated to Alexa Fluor were used 1:200 (AF488: anti-mouse A-11029, anti-rabbit A11008; AF555: anti-rabbit A-21429; AF647: anti-rabbit A21245, anti-mouse A-21236,) from Thermo Fisher Scientific, anti-sheep AF647 (ab150179) from Abcam. HRP-conjugated goat anti-mouse (A-5278), anti-rabbit (A-6154) were from Sigma and used 1:10,000. Protein A conjugated to 5 or 10 nm gold particles (PAG; used 1:50; Cell Microscopy Center, Utrecht University Hospital, Utrecht, Netherlands).

The sense strand for the indicated double-stranded siRNAs were synthesized with the following sequences (Qiagen): siCtrl, 5′-AATTCT CCG AAC GTG TCA CGT-3′; siCD63, 5’-AAGTTCTTGCTCTACGTCCTC-3’.

CD63-E217Q was constructed by Gibson Assembly using the primer pairs CD63E217Q_fwd 5’-CTTGGAATTGCTTTTGTCcAGGTTTTGGGAATTGTCTTTG-3’ and CD63E217Q_rev 5’- CAAAGACAATTCCCAAAACCTgGACAAAAGCAATTCCAAG-3’ and AmpR_fwd 5’-CTCATGGTTATGGCAGCACTGCATAATTCTCTTACTGTC-3’ and

AmpR_rev 5'-GACAGTAAGAGAATTATGCAGTGCTGCCATAACCATGAG-3'
on the parental vector pCDNA3.1-CD63 (CD63-WT) (kind gift from Kei Sato, University of Tokyo).
Mann-II-mCherry-pCMV, Lamp1-mCherry-pCMV and VSVG-EGFP-RUSH were kindly provided by Gaëlle Boncompain and Franck Perez (Institut Curie, Paris, France), D4-mCherry was kindly provided by Fabien Alpy (IGBMC, Illkirch, France)[92].

sEV isolation and characterization

sEVs were prepared from conditioned media incubated for 48h on sub-confluent cells. FBS supplemented medium was previously centrifuged at 100,000 g for 16h to remove FBS-derived EVs. Conditioned media were centrifuged at 300 g (15 min, 4° C) and 2000 g (20 min, 4°C) to remove cell debris.
For isolation by differential ultracentrifugation (UC), the supernatant (post 2000 g) was centrifuged at 10,000 g (30 min, 4°C) and sEVs were collected from the supernatant by centrifugation at 100,000 g (60 min, 4°C, 45Ti or 70Ti rotor, Beckman Coulter). The pellet was washed in PBS (pH 7) by centrifugation at 100,000 g (60 min, 4°C) and finally resuspended in PBS (pH 7).
For isolation by size exclusion chromatography (SEC), the supernatant (post 2000 g) was concentrated by ultrafiltration on a 10,000 MWCO filter (Centricon, Merck-Millipore) to obtain a concentrated conditioned media (CCM). sEVs were then isolated by SEC (IZON Science). Fractions from 7 to 9 were collected, pooled, and concentrated again using a 10,000 MWCO filter (Centricon, Merck-Millipore).
EV samples were used right after isolation or stored at -80°C.
For D4-GFP staining of sEVs, CCM (obtained as above) was incubated with D4-GFP (dilution 1:1000) overnight at 4°C under rotation and then fixed with 2% PFA for 15 minutes. sEVs were then isolated by SEC as described above. The samples were then processed for electron microscopy as described below.

Nanoparticle-tracking analysis

NTA measurements of EV size and concentration were performed using a ZetaView®, Particle Metrix. Samples were pre-diluted with filtered PBS and measured at 11 different positions for 2 cycles at 24°C. The videos were then processed by the ZetaView Software (version 8.04.02 SP).

Dynamic Light Scattering

DLS measurement of EV concentration was performed using Zetasizer Ultra®, Malvern Panalytical and ZS XPLORER (version 2.0.0.98) acquisition software. Samples were loaded in low-volume quartz batch ZEN 2112 cuvette (Hellma® Analytics, QS High Precision Cell, light path 3x3 mm) for analysis at room temperature with a dispersant scattering value of 82. Distributed particle concentration was measured.

Western Blot

Cells were lysed on ice in lysis buffer (20 mM Tris, 150 mM NaCl, 1% Triton X-100, and 1 mM EDTA, pH 7.2) supplemented with a protease inhibitor cocktail (Roche). Cell lysates or EVs were incubated with sample buffer with or without 350 mM 2-mercaptoethanol (Sigma), incubated at 60°C for 30 min, loaded on 4–12% Bis-Tris gels (Nu-PAGE, Invitrogen), and transferred on nitrocellulose membranes (GE Healthcare). Membranes were blocked in PBS/0.1% Tween (PBS/T) with 5% nonfat dried milk, incubated with indicated primary and secondary antibodies diluted in PBS/T-milk. Western blots were developed using the ECL SuperSignal West Pico or Dura (Thermo Fisher Scientific). Signal intensities were quantified with Image J Fiji software (version 2.1.0/1.53c or 1.54f).

Immunofluorescence and microscopy

Cells were grown on coverslips and fixed for 20 minutes at RT with 4% PFA/PBS and quenched for 10 min with PBS/50 mM glycine. Cells were incubated with PBS/0.2% BSA/0.1% saponin before incubation with primary and secondary antibodies in the same buffer. For ApoE staining, cells were fixed with cold methanol for 5 min at -20°C and IF was performed using PBS/0.2% BSA. Incubation with phalloidin AF-647 was performed during the secondary antibody incubation.

For CI-M6PR pulse-chase, cells grown on coverslips were incubated for 15 minutes at RT with anti-CI-M6PR antibody in complete media, washed with PBS and incubated at 37°C for 1h to allow antibody internalization. Cells were fixed as described above and processed for IF with a secondary antibody anti-mouse.

For VSVG-RUSH experiment, cells grown on coverslips were transfected with VSVG-EGFP-RUSH. After 20 h, D-biotin (40 µM, T=0) was added, cells were fixed at T=15, 30 or 60 minutes.

For Nile Red staining, cells were grown on coverslips and fixed as above. Cells were incubated with Nile Red for 5 minutes.

Coverslips were mounted using Prolong Gold antifade reagent with DAPI (Invitrogen).
Coverslips were analyzed on a wide-field microscope (Eclipse 80i Upright; Nikon) equipped with a CCD camera (CoolSNAP HQ2; Photometrics) using a 100x 1.4 NA Plan-Apo objective lens. Z images series were acquired every 0.2 µm with the piezoelectric motor (Physik Instrumente) using MetaMorph software (Molecular Devices, version 7.8.0.0). Raw images were deconvolved with Meinel algorithm (PICT-IBiSA imaging platform at Institut Curie).
For super-resolution microscopy (SR-IFM), cells were analyzed as previously described[93]. Briefly, images were acquired on a spinning disk system (Gataca Systems) based on an inverted microscope (Ti-E; Nikon) equipped with a sCMOS camera (Prime 95B; Photometrics), a confocal spinning head (X1; Yokogawa), a 100x 1.4 NA Plan-Apo objective lens, and a superresolution module (Live-SR; Gataca systems) based on structured illumination with optical reassignment technique and online processing leading to a two-time resolution improvement. MetaMorph software (Molecular Devices, version 7.8.0.0) was used.
For TopFluor Cholesterol (TF-chol) staining, cells were grown on coverslips in LPDS medium and incubated with TF-chol at 1 µM for 16h.
For LDL-BODIPY endocytosis, cells were grown on coverslips in LPDS medium and incubated with 4 µg/mL LDL-BODIPY for 16h before fixation.
For filipin staining, cells were grown on coverslips in LPDS medium and treated or not with U18666A at 1 µM for 16h before fixation. Coverslips were then incubated with Filipin III at 50µg/mL for 1h at RT in the dark before mounting. Coverslips were observed on a Leica 3D widefield 3D DEC microscope with a 100x 1.4 NA HCX Plan-Apo objective lens using a Metamorph (Molecular Devices) software.
For D4-GFP staining, cells were grown on coverslips in LPDS medium and treated or not with U18666A at 1 µM for 16h followed by D4-GFP staining as previously described[92]. Briefly, for non-permeabilized cells, coverslips were incubated with D4-GFP for 30 minutes at 37°C before fixation and mounting. For permeabilized cells, cells were fixed, and permeabilized in liquid nitrogen before D4-GFP incubation, CD63 antibody staining and mounting. Images were acquired using a confocal microscope Leica SP5 equipped with a 63x 1.4 NA objective using a LAS-AF software (Leica version 2.7.3.9723).

Electron Microscopy

For conventional electron microscopy, cells were seeded on coverslips and fixed with 2.5 % glutaraldehyde in 0.1 M cacodylate buffer. Cells were processed for Epon (TAAB Laboratories

Equipment) embedding as described[94] and ultrathin sections were contrasted with uranyl acetate and lead citrate.

For high-pressure freezing, cells were cultured on carbonated sapphire disks, high-pressure frozen with HPM100 (Leica Microsystems) and then freeze substituted in anhydrous acetone containing 1% OsO4/2% H2O for 64h in a freeze substitution system (AFS; Leica Microsystems). Cells were embedded in Epon and processed for sectioning and contrasting with uranyl acetate and lead citrate.

For ultrathin cryosections and immunogold labeling, cells were grown on flasks and fixed with 2% PFA/ 0.125% glutaraldehyde/ 0.1 M phosphate buffer. Cell pellets were embedded in 10% gelatin and infused in 2.3M sucrose. Gelatin blocks were frozen and processed for ultracryomicrotomy. Ultrathin sections were immunogold labeled using PAG 5 or 10 nm as previously described[82]. For cholesterol labeling, ultrathin sections were directly incubated for 30 min with D4-GFP (dilution 1:500), fixed with 1% glutaraldehyde and immunogold labeled using an antibody anti-GFP and PAG 10 nm.

EVs were directly deposited on formvar/carbon coated copper/palladium grids for 20 min at RT, fixed with PFA 2%/0.1 M phosphate buffer and processed for immunogold labeling as for cells.

Negative staining of cell ultrathin cryo-sections or EVs was performed using uranyl acetate 0.4% in methylcellulose.

The samples were analyzed with an 80 kV transmission electron microscope (Tecnai Spirit G2; Thermo Fischer, Eindhoven, The Netherlands) equipped with a 4k CCD camera (Quemesa, EMSIS, Münster, Germany) using the software iTEM (v.5.2; EMSIS).

Proteomic analysis

Sample preparation: HeLa or MNT-1 cells were cultured in media supplemented with LPDS for 48 hours, and lysed in freshly prepared urea buffer (8 M urea, 200mM ammonium bicarbonate). sEVs were isolated by SEC, fractions 7 to 9 were collected, pooled, centrifuged at 100,000g for 1h at 4°C, and the pellets were lysed in freshly prepared urea buffer. After sonication, lysates were quantified by *BCA* (ThermoScientific) or Nanodrop at 280nm wavelength (Mettler Toledo).

After vacuum concentration to dryness, sEV samples were diluted in 20µl of 8 M urea, 200mM ammonium bicarbonate. Cell lysates and sEV samples were then reduced with 5 mM DTT for 1 h at 37 °C and alkylated with 10 mM iodoacetamide for 30 min at room temperature in the dark. Samples were then diluted in 200mM ammonium bicarbonate to reach a final

concentration of 1 M urea and digested overnight at 37 °C with Trypsin/Lys-C (Promega CAT#: V5071) at a ratio of 1/50 for proteome samples and with 0.2 µg of Trypsin/LysC for sEVs. 5µg of proteomes or EVs were then loaded onto a homemade C18 StageTips for desalting. Peptides were eluted using 40/60 MeCN/H2O + 0.1% formic acid and vacuum concentrated to dryness. Peptides were reconstituted in 10 µl of injection buffer in 0.3% trifluoroacetic acid (TFA) before liquid chromatography-tandem mass spectrometry (LC-MS/MS) analysis.

LC-MS/MS Analysis: Online chromatography was performed with an RSLC nano system (Ultimate 3000, Thermo Scientific) coupled to an Orbitrap Exploris 480 mass spectrometer (Thermo Scientific). Peptides were trapped on a C18 column (75 µm inner diameter × 2 cm; nanoViper Acclaim PepMap™ 100, Thermo Scientific) with buffer A (2/98 MeCN/H2O in 0.1% formic acid) at a flow rate of 3.0 µL/min over 4 min. Separation was performed on a 50 cm x 75 µm C18 column (nanoViper Acclaim PepMap™ RSLC, 2 µm, 100Å, Thermo Scientific) regulated to a temperature of 40°C with a linear gradient of 3% to 29% buffer B (100% MeCN in 0.1% formic acid) at a flow rate of 300 nL/min over 91 min for the EV analyses and a linear gradient of 3% to 32% buffer B over 211min for the cell proteome analyses. MS full scans were performed in the ultrahigh-field Orbitrap mass analyzer in ranges m/z 375–1500 with a resolution of 120 000 (at m/z 200). The top 20 most intense ions were subjected to Orbitrap for EV proteome analyses and top 30 for cell proteomes for further fragmentation via high energy collision dissociation (HCD) activation and a resolution of 15 000 with the AGC target set to 100%. We selected ions with charge state from 2+ to 6+ for screening. Normalized collision energy (NCE) was set at 30 and the dynamic exclusion to 40s.

Data analysis: For identification, the data were searched against the *Homo Sapiens* (UP000005640) UniProt database using Sequest HT through proteome discoverer (version 2.4). Enzyme specificity was set to trypsin and a maximum of two miss cleavages sites were allowed. Oxidized methionine, Met-loss, Met-loss-Acetyl and N-terminal acetylation were set as variable modifications. Maximum allowed mass deviation was set to 10 ppm for monoisotopic precursor ions and 0.02 Da for MS/MS peaks. The resulting files were further processed using myProMS v3.9.3[95] (https://github.com/bioinfo-pf-curie/myproms). FDR calculation used Percolator[96] and was set to 1% at the peptide level for the whole study. The label free quantification was performed by peptide Extracted Ion Chromatograms (XICs), reextracted across all conditions and computed with MassChroQ version 2.2.21[97]. For protein quantification, XICs from proteotypic peptides shared between compared conditions (TopN matching) and missed cleavages were allowed. Median and scale normalization was applied on the total signal to correct the XICs for each biological replicate (N=5 for WT and N=10 for

CD63 KO by combining two KO clones). To evaluate the statistical significance of the change in protein abundance, a linear model (adjusted on peptides and biological replicates) was performed, and a two sided T-test was applied on the fold change estimated by the model. The p-values were then adjusted using the Benjamini–Hochberg FDR procedure. Proteins with at least two distinct peptides in three replicates of a same state, a 2-fold enrichment and an adjusted p-value ≤ 0.05 were considered significantly enriched in sample comparisons. Proteins unique to a condition were also considered if they matched the peptides criteria. Proteins selected with these criteria were further subjected to Gene Ontology (GO) functional enrichment analysis as in[98] by using the complete gene ontology file. The mass spectrometry proteomics raw data have been deposited to the ProteomeXchange Consortium via the PRIDE[99] partner repository.
Links for publicly accessible source data are listed in the Data Availability Statement and in Source Data files.

Lipidomic analysis

Sample preparation: HeLa or MNT-1 cells were cultured in media supplemented with LPDS for 48 hours and sEVs were isolated by SEC as described above while cell pellets were resuspended in 100 µl methanol.
80 µl of cell homogenate or total volume of EVs in suspension (150 µl) was supplemented with a mixture of internal standards, and lipids were extracted with 700 (cells) or 800 (EVs) µl methanol and 400µl chloroform in the presence of the antioxidant BHT and 310µl (cells) or 160µl (EVs) of HCl 0,01N. Phase separation was triggered by addition of 400 µl chloroform and 400 µl water. Samples were vortexed for 1 min, centrifuged at 3600g for 10min at 4°C. Lower phase containing the lipids was dried and resuspended in 40 µl of chloroform/acetonitrile/isopropanol (80:19:1 v/v). Quality controls (control serum independent of the study) were extracted in parallel of the samples.
LC(HILIC)-MS/MS analysis of phospho- and sphingolipids: Phospho- (PL) and sphingolipids (SL) were quantified by LC-(ESI)MS/MS using a Prominence UFLC (Shimadzu, Tokyo, Japan) and a QTrap 4000 mass spectrometer (AB Sciex, Framingham, MA, USA). Quantification of phospholipids and sphingolipids was performed in positive-ion mode. Sample (4µl) was injected into a Kinetex HILIC column (150x2.1mm, 2.6µm) (Phenomenex, CA, USA). Mobile phases consisted of (A) 30mM ammonium acetate and 0.2% acetic acid and (B) acetonitrile supplemented with 0.2% acetic acid. Lipid species were detected in positive ionization mode using scheduled multiple reaction monitoring (sMRM) reflecting their head group fragmentation for PL and sphingomyelin (SM) (PIS (product ion scan) 184m/z for PC,

LPC and SM, NL (neutral loss) 141m/z for PE, PIS (RCO+PE) for PE-P, NL 277m/z for PI, NL 185m/z for PS, NL 172m/z for LPG, NL (BMP head+R) for BMP, NL 189m/z for PG, NL 115m/z for PA) and sphingoid base fragmentation for ceramides (PIS 266m/z and PIS 264m/z). Three independent injections were used: one injection for very minor lipids (PS, PA, LPC and LPE), one injection for the other lipids (PG, BMP, LPG, PE, PI, SM, ceramides, DHC), one injection for abundant lipids following sample dilution (PC and some SM).

LC(C18)-MS/MS analysis of neutral lipids: Cholesteryl esters (CE) and free cholesterol were quantified by LC-(ESI) MS/MS using a Prominence UFLC and a QTrap 4000 mass spectrometer. Quantification of CE and cholesterol was performed in positive-ion mode. Sample (4µl) was injected into an Ascentis C18 column (150x2.1mm, 2.7µm). Mobile phases consisted of (A) acetonitrile/water (60:40 v/v) and (B) isopropanol/acetonitrile (90:10 v/v) supplemented with 10mM ammonium formate and 0.1% formic acid. Lipid species were detected using scheduled multiple reaction monitoring (sMRM) reflecting the fragmentation of the cholesterol core (PIS 369m/z).

Data pre-processing: An in-house developed R script adapted from Ejsing et al[100] was used to correct for isotopic contribution to MRM signals in HILIC mode. Lipid features whose variability exceeded 30% in quality controls were discarded. Data were expressed normalized to total lipid signal (mol% of total lipids). This normalization was preferred for the statistical analysis as it allowed the comparison of cells and EV lipid composition and was independent of the size of the particles.

Statistical Analysis: The statistical analysis of the lipidomics data were performed using Multi Experiment Viewer (MeV) statistical software package (version 4.9.0; http://www.tm4.org/mev/)[101]. Data are shown as mean ± SEM. Comparisons of the groups were performed by a 2 two-tailed Student's t-test. Features were considered significant when the p value was below 0.05 after Benjamini-Hochberg[102] for false discovery rate (FDR) correction.

Cholesterol levels measurement

Cells were grown in LPDS for 48h, EVs were isolated by SEC, and cells lysed. Amplex Red Cholesterol assay kit (Invitrogen, ThermoFisher Scientific) was used according to the manufacturer's protocol. Equal amount of EVs and cell lysate were loaded. For EVs, cholesterol content is reported as a ratio of the amount of cholesterol per EV.

Alignment of tetraspanin sequences

Sequences of CD63 (P08962), CD81 (P60033), and CD9 (P21926) were obtained from Uniprot and alignment was performed using CLUSTAL O (1.2.4).

3D structure of CD63 and interaction with cholesterol

A 3D structure of CD63 WT was predicted using the I-TASSER on-line server suite[103] by interrogating the server with CD63 (P08962) sequence for modelisation. Models were ranked based on their I-TASSER confidence (C) score (range 5 to +2 with a higher score correlating with an improved model). The model of prediction with the highest (C) score was selected (C=0,23).

Molecular docking of cholesterol with CD63

The interaction between CD63 and cholesterol was modeled with Haddock 2.4 on-line server suite[104] by interrogating the server with the CD63 WT or E217Q 3D structures obtained from I-TASSER and a cholesterol molecule. CD63 residues were classified as active in cholesterol binding based upon CD81 residues previously implicated in cholesterol binding[34].

Atomic force microscopy

Sample preparation: HeLa cells were cultured in media supplemented with LPDS for 48 hours and sEVs were isolated by SEC as described above.

AFM experiments: AFM experiments and data analysis were performed as described in detail previously[55,105]. sEVs were deposited on poly-L-lysine (PLL) coated glass coverslips prepared as follows. First, the coverslips were cleaned by immersing them in a 96% ethanol, 3% concentrated HCl solution for 10 min, and rinsed with ultrapure water. Then, coverslips were coated for 1 h in a 0.001 % poly-L-lysine (Sigma) solution, rinsed twice with ultrapure water, and dried at 37 °C overnight. The coated coverslips were stored at 7 °C and used for a maximum of 1 month. A PLL-coated coverslip was glued to a glass slide using conventional transparent superglue or two-component epoxy glue. After that, a glass ring was glued on top of the coverslip using JPK bio-compatible glue (Bruker) to hold the imaging buffer in place. The sEV sample was vortexed for ~5 s before 10 µl of sample were added to the center of the PLL-coated coverslip. After filling the chamber with PBS (imaging buffer), sEVs were imaged in QI mode on a JPK NanoWizard Ultra Speed setup situated on an inverted microscope (Olympus). The force set point during imaging was typically <100 pN, pixel time was set to 8.0 ms and z-length was set to 50-80 nm. Imaging was performed at room temperature (~22 °C). After imaging a single particle, the particle was indented at its center first with a maximum force of 0.4-0.5 nN,

and then directly multiple times (typically 5 times) with higher forces (5-6 nN). The extend and retract speed of the cantilever during indentation was set to 0.3 µm/s throughout all experiments. z-Length during indentation was 500 nm, sampling rate was set to 1024 Hz and the z-loop was closed. Both before and after indentation of the particle, the tip was checked for contamination and linear response by pushing it on the glass surface until a set force of 5 - 6 nN was reached, recording a force distance curve. After indentation, another image was recorded to check for movement or collapse/changes of the particle. Only particles exceeding a minimum height (25 nm) were indented to avoid indenting stacks of multiple bilayers. Quartz-like cantilevers and tips were used with a nominal tip radius of <10 nm and a cantilever stiffness of 0.06 N/m, as specified by the manufacturer (qp-BioAC, Nanosensors). Individual cantilevers were calibrated using thermal tuning.

AFM image analysis: Images were processed using JPK Data Processing Software. Cross sections were taken for each particle along the fast-scanning axis in order to analyze the shape and the size of the particle. The radius of curvature R_c was obtained by fitting a circular arc to the data above half of the maximum height of the spherical cap and correcting for the tip radius (10 nm as provided by the manufacturer). The height obtained from the fit was compared to the height obtained from the force indentation curve to ensure indention at the particle's center. Recorded force distance curves were corrected for the offset using JPK Data Processing Software and subsequently exported for further analysis in Origin (version 2019). Assuming surface area conservation allowed us to calculate the radius R_0 of the particles in solution, as described previously[55,105].

AFM FDC analysis: A linear fit was performed on the cantilever response measured on the PLL-coated glass coverslip. This result was used to transform the measured response into force indentation curves (FDCs) (see also[105]). The contact point was found manually. By fitting a straight line to the data in the range 0.02–0.1 R_c the stiffness of the sEVs was obtained. For determining the tether force two lines with slope 0 were fit individually to the last detachment of the tip in the retraction curve before reaching the baseline again. The difference of the two intersects with the y-axis was calculated yielding the tether force. Only adhesion events exceeding the contact point were identified as tethers and were included. Tether forces > 0.25 nN were excluded because these could correspond to multiple bilayer tethers, as reported previously[56]. For fitting to the theory, described in detail elsewhere[55,105], the sum of the squared log Euclidian distance between the theoretical curve and the individual experimental data points was minimized by adjusting κ as a single fitting parameter. Confidence intervals were estimated using the bias corrected percentile method with 500 bootstrapping repetitions, for which a set

of observed value combinations equal in size to the original data set was randomly drawn and fitted.

EV uptake experiment

Producing cells were grown in LPDS and incubated with TF-chol for 16h at 1 uM. Fresh media (without TF-chol) was added and sEVs were prepared from conditioned media after 32h. EVs were isolated by UC and labeled or not with Membright 640 (Idylle, Lipilight) as previously described[106]. Recipient cells were treated or not with U18666A overnight at 1 µM and fed with EVs from producing cells (considering a ratio of 5 producing cells for 1 recipient cell) for 24h hour before fixation and imaging with a confocal microscope Leica SP5 with a 63x 1.4 NA objective. Z-stack images were acquired every 0,18 µm.

Image analysis and quantifications

ImageJ Fiji software (version 2.1.0/1.53c or 1.54F) was used.

Manders' and Pearson's correlation coefficient

Manders' and Person`s correlation coefficients between two channels were quantified using JACoP plugin of ImageJ Fiji.

Phalloidin fluorescence on endosomes

Average intensity z projections of five stacks (acquired every 0.20 µm) were generated for both LAMP-1 or EEA1 and phalloidin channel. 15-pixel (1,65 nm)-diameter circles were drawn around LAMP-1- or EEA1-positive endosomes (ROI). The ROI was copied in the phalloidin channel and phalloidin mean fluorescence intensity in the ROI was measured using ImageJ Fiji.

LDL-BODIPY, D4-GFP, pD4-mCherry,TF-chol, MemBright fluorescence intensity

The mean intracellular fluorescence intensity or the integrated density was measured by manually selecting an area covering the entire cell with ImageJ Fiji.

Filipin fluorescence intensity

For each cell, the ratio of maximum intensity of fluorescence was measured by dividing the maximum intensity in U18666A treated cells compared to the DMSO treated cells. Data are presented as a percentage of enrichment of filipin intensity of fluorescence in U18666A treated cells compared to the DMSO control.

Size, number, and distribution of TF-chol compartments

Size and number of TF-chol compartments were measured by thresholding the intensity of fluorescence within the cells and analyzing particles with ImageJ Fiji. For the distribution of TF-chol compartments, ROI of interest were drawn around the nucleus and enlarged to locate

TF-chol compartments within different areas of each cell from the perinuclear region to the plasma membrane. Data are presented as the percentage of perinuclear and peripheral compartments in the different conditions.

Localization of internalized antibody directed against CI-M6PR

Average intensity z projections of four stacks (acquired every 0,20 µm) were generated. The total intracellular fluorescence intensity was measured by manually selecting an area covering the entire cell. The fluorescence intensity within a 7 x 7 μm^2 region centered on the Golgi complex (TGN46 staining was used as reference) was then measured. The non-Golgi fluorescence (vesicular) intensity was obtained by subtracting the fluorescence intensity in the Golgi complex from the total fluorescence intensity. Data are presented as the non-Golgi/Golgi CIMPR fluorescence ratio from each cell.

Immunogold labeling

Quantification of immunogold labeling on ultrathin cryosections or EVs was performed by counting the number of gold particles per cell compartment or EV. MVEs were defined as compartments delimited by a membrane with numerous internal vesicles. The count was performed on randomly selected cells. As the D4-GFP staining can label free cholesterol that is not associated with membranes on EV samples, only the gold particles associated with EV membranes were quantified.

Statistics & Reproducibility

The experiments were not randomized and the investigators were not blinded to allocation during experiments and outcome assessment. Experiments were performed multiple times, and experiments included in Figure 1a, 1b, 1c, 6d, Extended Data Fig. 1a, 4c, 4g were performed independently by two different investigators.

No statistical method was used to predetermine sample size. No data were excluded from the analyses. For all assays, quantification and statistics were derived from n= 3 independent experiments, unless specified in the legends. For Fig. 4 b, Fig.5 d-f, Fig.6 f, g, Fig.7c, Fig. 8 a-c, ED Fig. 5g, ED Fig. 6c, ED Fig. 7 d, f, ED Fig. 8a, d, statistics were derived from n= number of cells pooled across 2 independent experiments. Experiments in Fig. 4a and ED 5d were performed once and statistics were derived from n= number of cells. Experiments shown in Fig. 1f, 6e, ED Fig.1e, ED Fig.5a, ED Fig.7a, ED Fig. 8d, ED Fig.9 b,c are representative of 2 independent experiments.

Data are presented as mean ± SEM, unless differently indicated in the legends. Statistics were calculated in GraphPad Prism 10 (version 10.2.1) using Student's t test, or Ordinary one-way

ANOVA, or Kruskal-Wallis test or Mann-Whitney test, unless specified. Significant differences between control or treated samples are indicated (****, P <0.0001; ***, P <0.001; **, P < 0.01; *, P < 0.05, ns P< 0.05).

Data availability

The mass spectrometry proteomics raw data have been deposited to the ProteomeXchange Consortium via the PRIDE partner repository. The datasets are publicly available at the following links: ProteomeXchange title: Human - Cells and Extracellular vesicles of Hela and MNT-1 WT vs CD63 KO Proteomes 1, ProteomeXchange accession: PXD037146, Project Webpage: http://www.ebi.ac.uk/pride/archive/projects/PXD037146 , FTP Download: https://ftp.pride.ebi.ac.uk/pride/data/archive/2024/04/PXD037146; ProteomeXchange title: Human - Cells and Extracellular vesicles of Hela and MNT-1 WT vs CD63 KO Proteomes 2 ProteomeXchange accession: PXD037147, Project Webpage: http://www.ebi.ac.uk/pride/archive/projects/PXD037147, FTP Download: https://ftp.pride.ebi.ac.uk/pride/data/archive/2024/04/PXD037147; ProteomeXchange title: Human - Cells and Extracellular vesicles of Hela and MNT-1 WT vs CD63 KO Exosomes ProteomeXchange accession: PXD037149, Project Webpage: http://www.ebi.ac.uk/pride/archive/projects/PXD037149, FTP Download: https://ftp.pride.ebi.ac.uk/pride/data/archive/2024/04/PXD037149.

UniProt accession codes are: Homo Sapiens (UP000005640), P08962 for CD63, P60033 for CD81, and P21926 for CD9.

Lipidomics datasets have been include in full in supplementary tables, provided in Source Data.

All relevant data are included in the paper.

Source data has been provided in Source Data. All other data supporting the findings of this study are available from the corresponding author on reasonable request.

Methods only references

91. Ran, F. A. *et al.* Genome engineering using the CRISPR-Cas9 system. *Nat. Protoc.* **8**, 2281–2308 (2013).

92. Wilhelm, L. P., Voilquin, L., Kobayashi, T., Tomasetto, C. & Alpy, F. Intracellular and Plasma Membrane Cholesterol Labeling and Quantification Using Filipin and GFP-D4. *Methods Mol. Biol. Clifton NJ* **1949**, 137–152 (2019).

93. Ripoll, L. *et al.* Myosin VI and branched actin filaments mediate membrane constriction and fission of melanosomal tubule carriers. *J. Cell Biol.* **217**, 2709–2726 (2018).
94. Raposo, G., Tenza, D., Murphy, D. M., Berson, J. F. & Marks, M. S. Distinct Protein Sorting and Localization to Premelanosomes, Melanosomes, and Lysosomes in Pigmented Melanocytic Cells✪. *J. Cell Biol.* **152**, 809–824 (2001).
95. Poullet, P., Carpentier, S. & Barillot, E. myProMS, a web server for management and validation of mass spectrometry-based proteomic data. *Proteomics* **7**, 2553–2556 (2007).
96. The, M., MacCoss, M. J., Noble, W. S. & Käll, L. Fast and Accurate Protein False Discovery Rates on Large-Scale Proteomics Data Sets with Percolator 3.0. *J. Am. Soc. Mass Spectrom.* **27**, 1719–1727 (2016).
97. Valot, B., Langella, O., Nano, E. & Zivy, M. MassChroQ: a versatile tool for mass spectrometry quantification. *Proteomics* **11**, 3572–3577 (2011).
98. Kowal, J. *et al.* Proteomic comparison defines novel markers to characterize heterogeneous populations of extracellular vesicle subtypes. *Proc. Natl. Acad. Sci. U. S. A.* **113**, E968-977 (2016).
99. Perez-Riverol, Y. *et al.* The PRIDE database and related tools and resources in 2019: improving support for quantification data. *Nucleic Acids Res.* **47**, D442–D450 (2019).
100. Ejsing, C. S. *et al.* Automated identification and quantification of glycerophospholipid molecular species by multiple precursor ion scanning. *Anal. Chem.* **78**, 6202–6214 (2006).
101. Saeed, A. I. *et al.* TM4: a free, open-source system for microarray data management and analysis. *BioTechniques* **34**, 374–378 (2003).
102. Benjamini, Y. & Hochberg, Y. Controlling the False Discovery Rate: A Practical and Powerful Approach to Multiple Testing. *J. R. Stat. Soc. Ser. B Methodol.* **57**, 289–300 (1995).
103. Zhang, Y. I-TASSER server for protein 3D structure prediction. *BMC Bioinformatics* **9**, 40 (2008).
104. van Zundert, G. C. P. *et al.* The HADDOCK2.2 Web Server: User-Friendly Integrative Modeling of Biomolecular Complexes. *J. Mol. Biol.* **428**, 720–725 (2016).
105. Vorselen, D., Piontek, M. C., Roos, W. H. & Wuite, G. J. L. Mechanical Characterization of Liposomes and Extracellular Vesicles, a Protocol. *Front. Mol. Biosci.* **7**, (2020).
106. Mary, B., Ghoroghi, S., Hyenne, V. & Goetz, J. G. Chapter Fourteen - Live tracking of extracellular vesicles in larval zebrafish. in *Methods in Enzymology* (eds. Spada, S. & Galluzzi, L.) vol. 645 243–275 (Academic Press, 2020).

1434

1435

Fig. 1

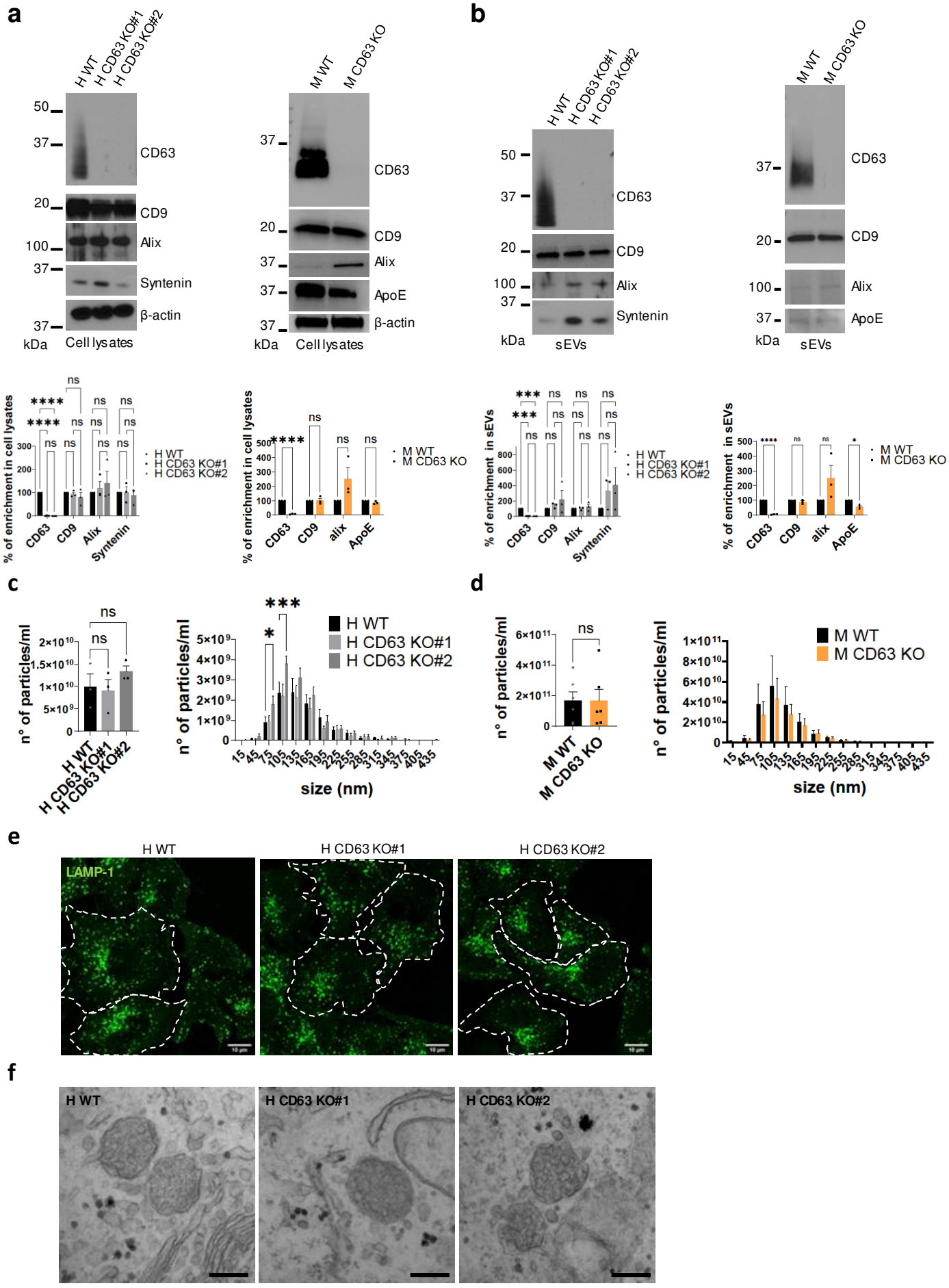
a
H WT
H CD63 KO#1
H CD63 KO#2
M WT
M CD63 KO
CD63
CD9
Alix
Syntenin
β-actin
ApoE
kDa
Cell lysates
b
sEVs
% of enrichment in cell lysates
% of enrichment in sEVs
c
n° of particles/ml
size (nm)
d
e
LAMP-1
f

Fig. 2

a

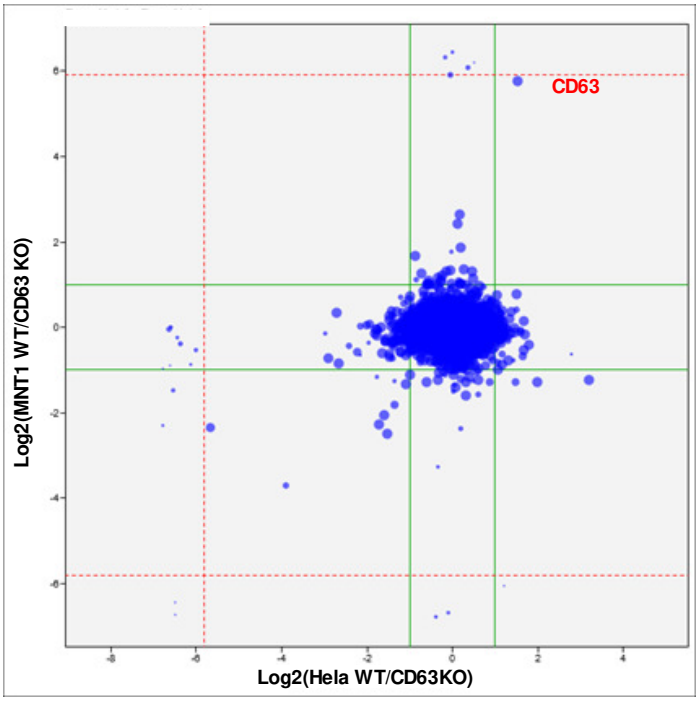

b

Protein Name	Hela WT/ CD63KO Ratio	MNT-1 WT/ CD63 KO Ratio	MW (kDa)	Description
P08962	2.88	54.45	25.6	CD63 antigen

c

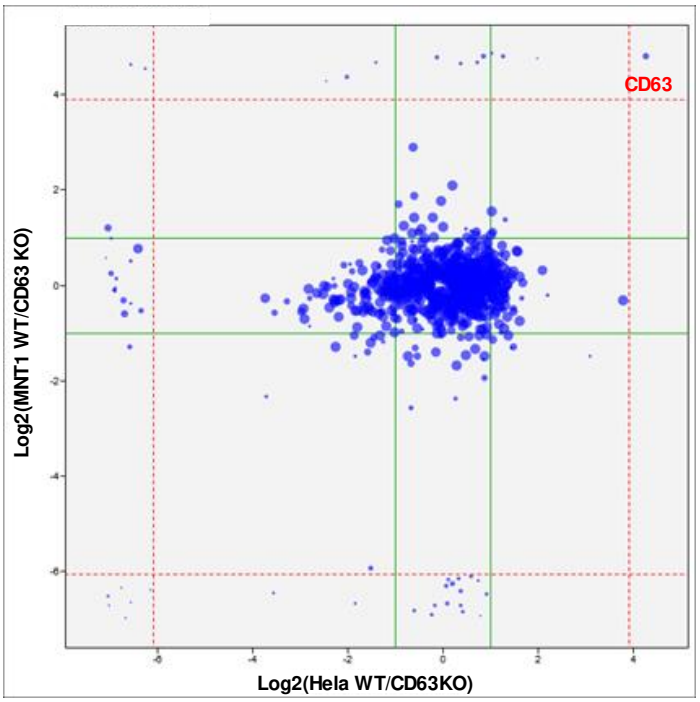

d

Protein Name	Hela WT/ CD63 KO Ratio	MNT1 WT/ CD63 KO Ratio	MW (kDa)	Description
O15427	2.04	∞	49.5	Monocarboxylate transporter 4
P08962	∞	∞	25.6	CD63 antigen
P0CW18	2.04	2.93	64.6	Serine protease 56
P43003	2.40	∞	59.6	Excitatory amino acid transporter 1
Q9BY44	2.07	2.17	65.0	Eukaryotic translation initiation factor 2A

GO Term	Enrichment Factor	P-value
Symporter activity	54,767	5,22E-04
Carboxylic acid transmembrane transporter activity	49,6	6,36E-04
Organic acid transmembrane transporter activity	49,6	6,36E-04
Organic anion transmembrane transporter activity	36,511	1,17E-03
Secondary active transmembrane transporter activity	33,136	1,42E-03

Fig. 3

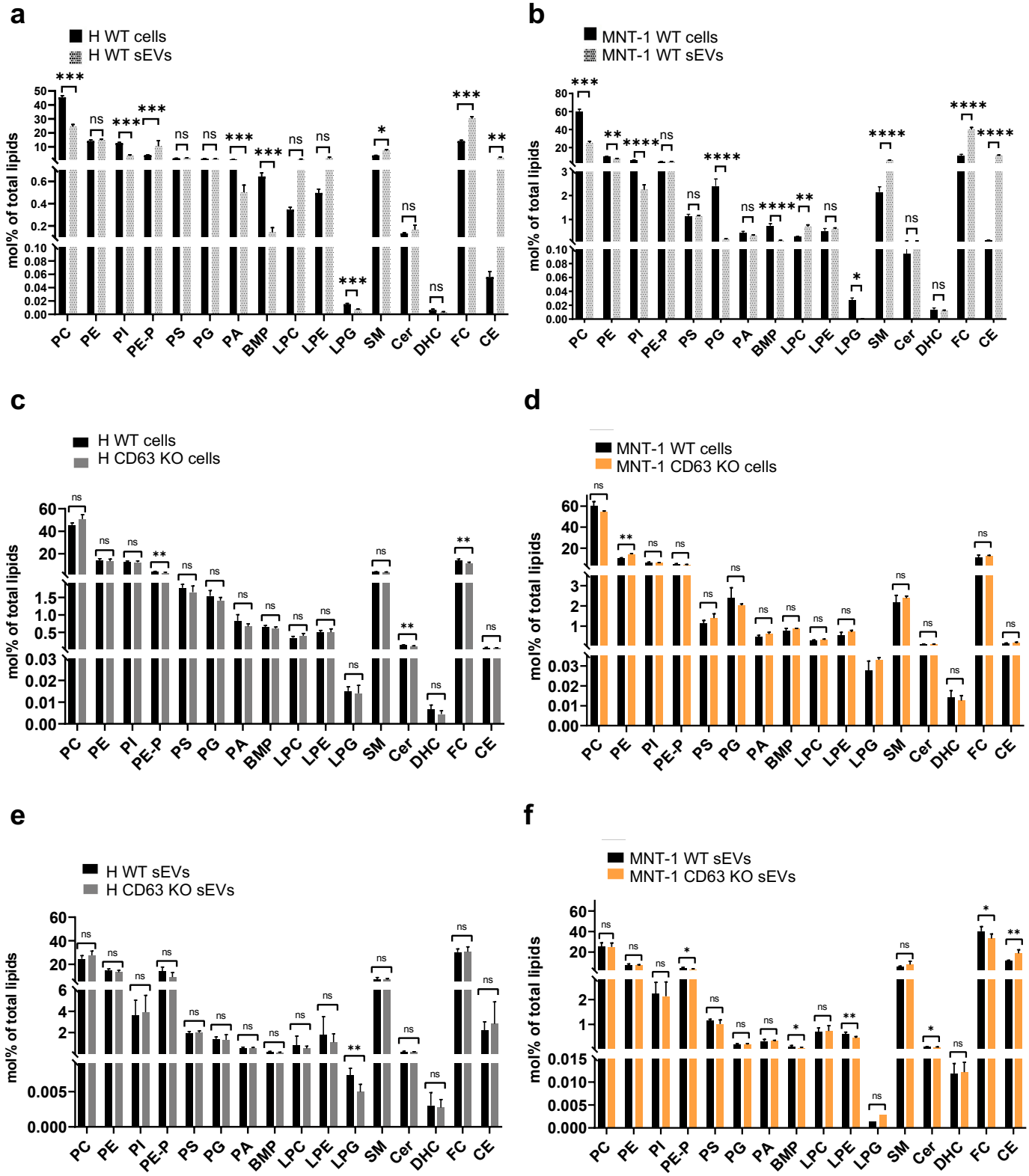
a
H WT cells
H WT sEVs
mol% of total lipids
PC PE PI PE-P PS PG PA BMP LPC LPE LPG SM Cer DHC FC CE
b
MNT-1 WT cells
MNT-1 WT sEVs
mol% of total lipids
PC PE PI PE-P PS PG PA BMP LPC LPE LPG SM Cer DHC FC CE
c
H WT cells
H CD63 KO cells
mol% of total lipids
PC PE PI PE-P PS PG PA BMP LPC LPE LPG SM Cer DHC FC CE
d
MNT-1 WT cells
MNT-1 CD63 KO cells
mol% of total lipids
PC PE PI PE-P PS PG PA BMP LPC LPE LPG SM Cer DHC FC CE
e
H WT sEVs
H CD63 KO sEVs
mol% of total lipids
PC PE PI PE-P PS PG PA BMP LPC LPE LPG SM Cer DHC FC CE
f
MNT-1 WT sEVs
MNT-1 CD63 KO sEVs
mol% of total lipids
PC PE PI PE-P PS PG PA BMP LPC LPE LPG SM Cer DHC FC CE

Fig. 4

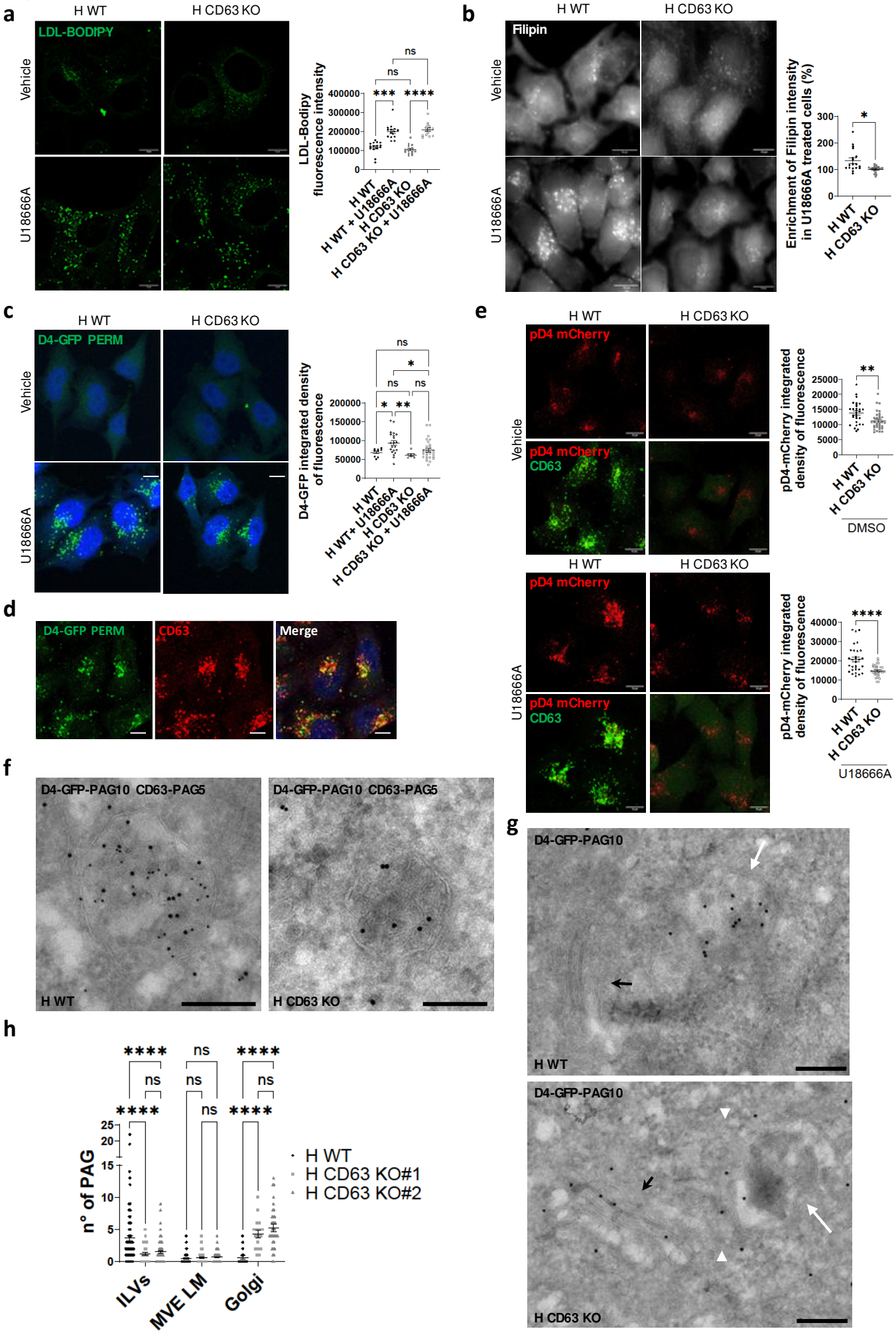
a
H WT
H CD63 KO
LDL-BODIPY
Vehicle
U18666A
LDL-Bodipy fluorescence intensity
ns
***
****
H WT
H WT + U18666A
H CD63 KO
H CD63 KO + U18666A
b
Filipin
Enrichment of Filipin intensity in U18666A treated cells (%)
*
c
D4-GFP PERM
D4-GFP integrated density of fluorescence
**
d
D4-GFP PERM
CD63
Merge
e
pD4 mCherry
pD4 mCherry
CD63
pD4-mCherry integrated density of fluorescence
DMSO
U18666A
f
D4-GFP-PAG10 CD63-PAG5
H WT
H CD63 KO
g
D4-GFP-PAG10
h
n° of PAG
ILVs
MVE LM
Golgi
H WT
H CD63 KO#1
H CD63 KO#2

Fig. 5

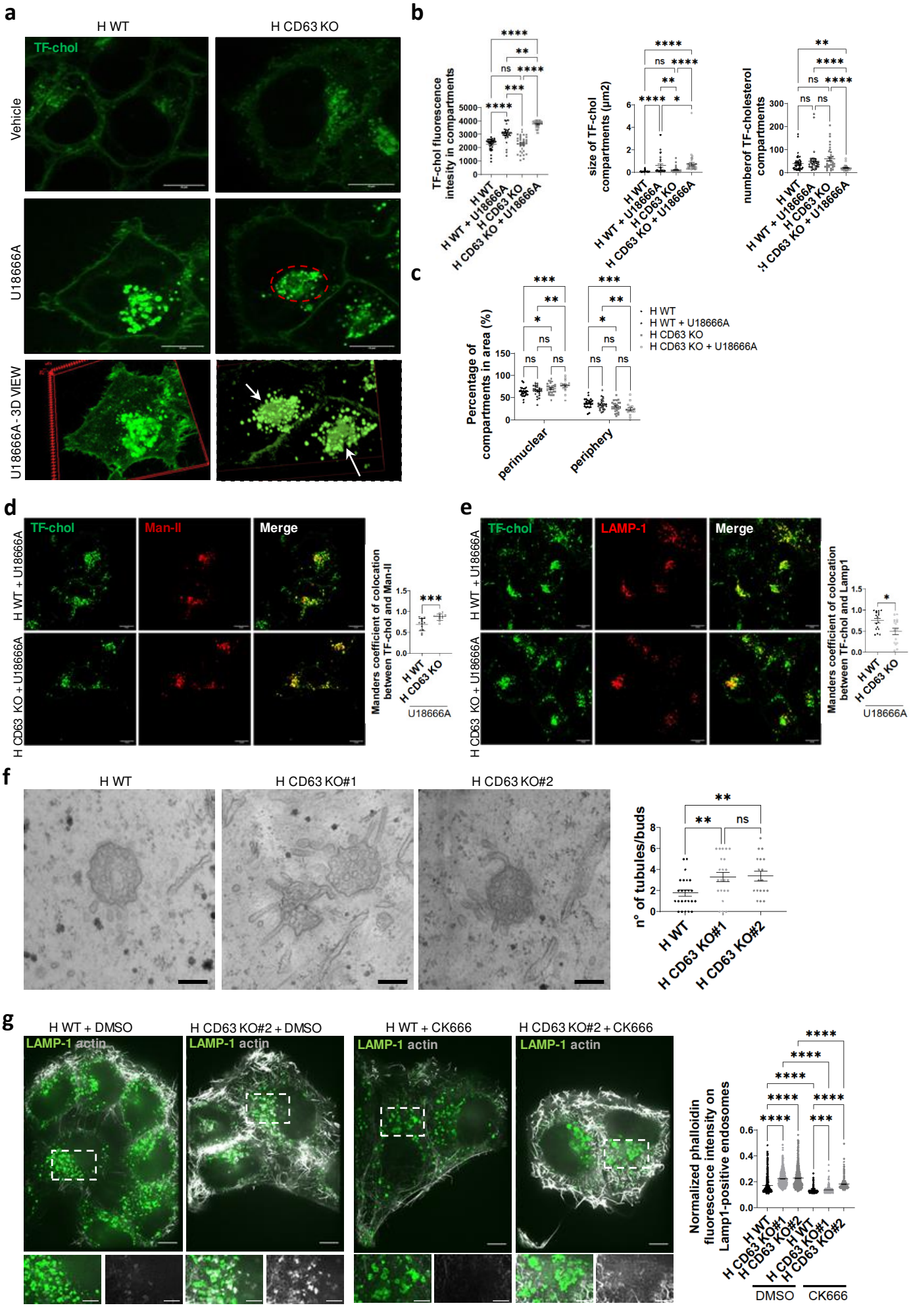
a
H WT
H CD63 KO
TF-chol
Vehicle
U18666A
U18666A - 3D VIEW
b
TF-chol fluorescence intesity in compartments
size of TF-chol compartments (µm2)
numberof TF-cholesterol compartments
H WT
H WT + U18666A
H CD63 KO
H CD63 KO + U18666A
c
Percentage of compartments in area (%)
perinuclear
periphery
d
TF-chol
Man-II
Merge
Manders coefficient of colocation between TF-chol and Man-II
e
LAMP-1
Manders coefficient of colocation between TF-chol and Lamp1
f
H CD63 KO#1
H CD63 KO#2
n° of tubules/buds
g
H WT + DMSO
H CD63 KO#2 + DMSO
H WT + CK666
H CD63 KO#2 + CK666
LAMP-1 actin
Normalized phalloidin fluorescence intensity on Lamp1-positive endosomes
DMSO
CK666

Fig. 6

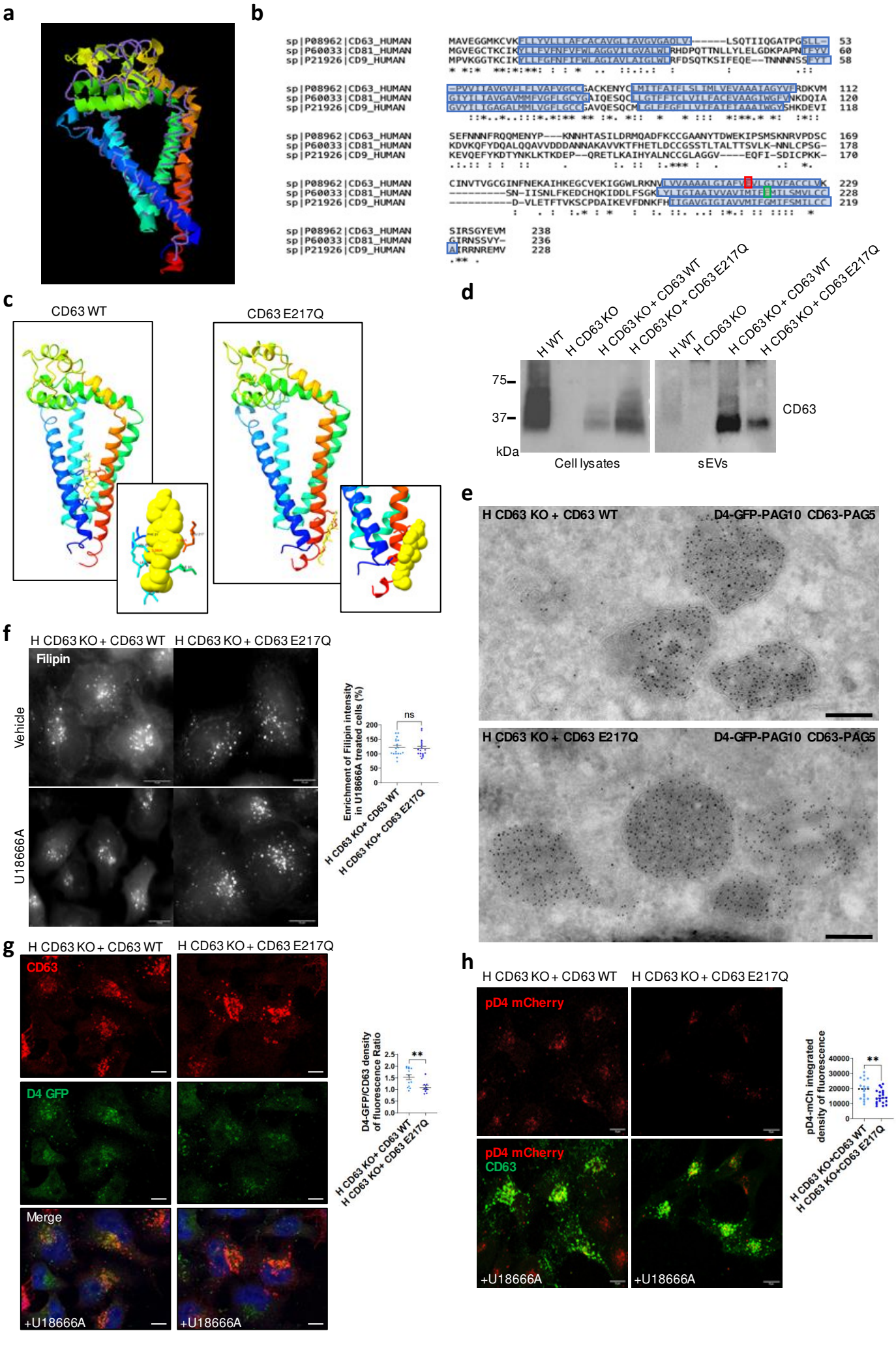
a
b
sp|P08962|CD63_HUMAN
sp|P60033|CD81_HUMAN
sp|P21926|CD9_HUMAN
c
CD63 WT
CD63 E217Q
d
H WT
H CD63 KO
H CD63 KO + CD63 WT
H CD63 KO + CD63 E217Q
75
37
kDa
CD63
Cell lysates
sEVs
e
H CD63 KO + CD63 WT
D4-GFP-PAG10 CD63-PAG5
H CD63 KO + CD63 E217Q
f
H CD63 KO + CD63 WT
H CD63 KO + CD63 E217Q
Filipin
Vehicle
U18666A
Enrichment of Filipin intensity in U18666A treated cells (%)
ns
g
CD63
D4 GFP
Merge
+U18666A
D4-GFP/CD63 density of fluorescence Ratio
**
h
pD4 mCherry
CD63
pD4-mCh integrated density of fluorescence

Fig. 7

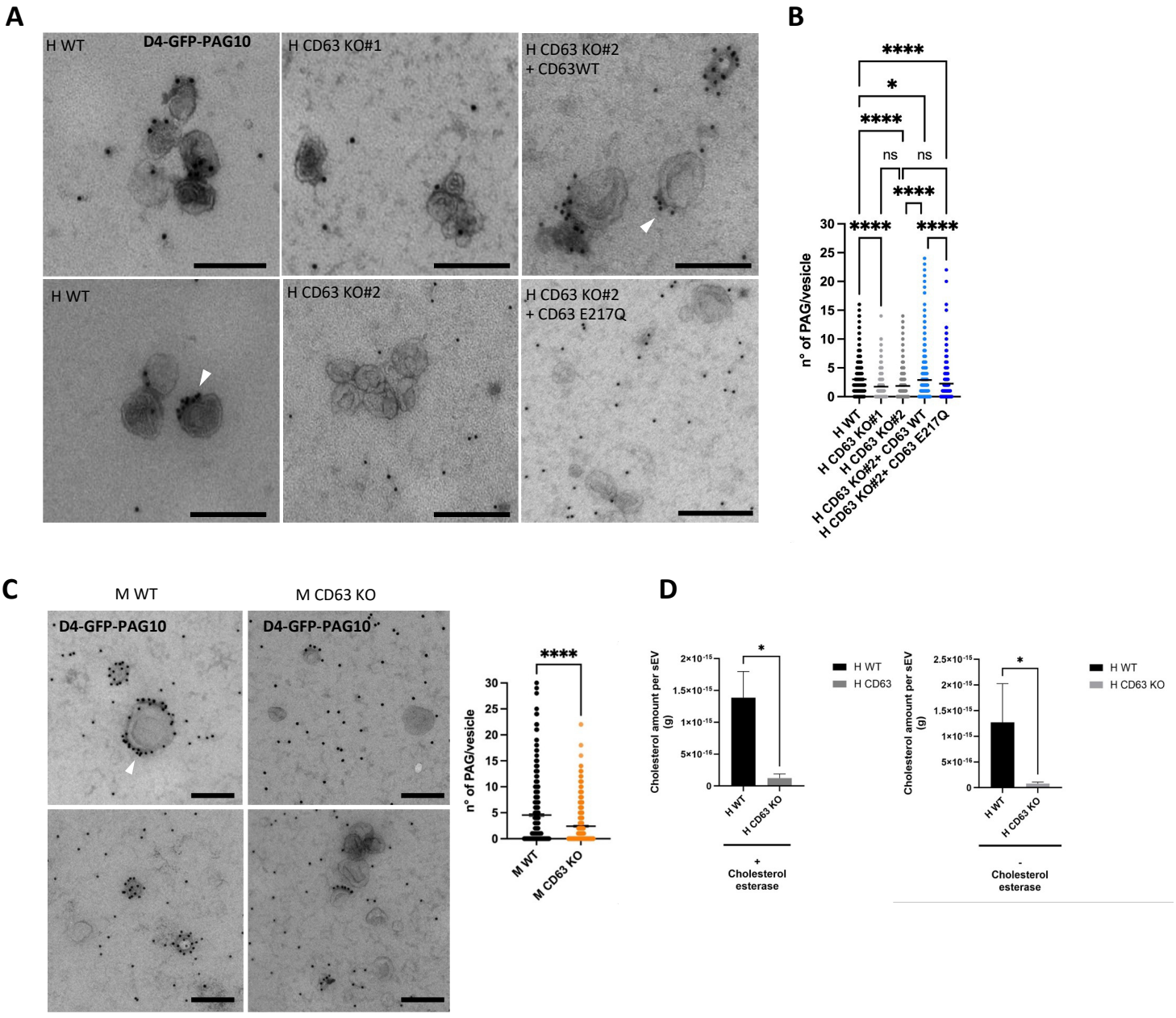
A
H WT
D4-GFP-PAG10
H CD63 KO#1
H CD63 KO#2
+ CD63WT
H WT
H CD63 KO#2
H CD63 KO#2
+ CD63 E217Q
B
****
*
****
ns
ns
****
****
****
n° of PAG/vesicle
30
25
20
15
10
5
0
H WT
H CD63 KO#1
H CD63 KO#2
H CD63 KO#2+ CD63 WT
H CD63 KO#2+ CD63 E217Q
C
M WT
M CD63 KO
D4-GFP-PAG10
D4-GFP-PAG10
****
n° of PAG/vesicle
30
25
20
15
10
5
0
M WT
M CD63 KO
D
Cholesterol amount per sEV (g)
2×10⁻¹⁵
1.5×10⁻¹⁵
1×10⁻¹⁵
5×10⁻¹⁶
0
*
H WT
H CD63 KO
+
Cholesterol esterase
H WT
H CD63
Cholesterol amount per sEV (g)
2.5×10⁻¹⁵
2×10⁻¹⁵
1.5×10⁻¹⁵
1×10⁻¹⁵
5×10⁻¹⁶
0
*
H WT
H CD63 KO
-
Cholesterol esterase
H WT
H CD63 KO

Fig. 8

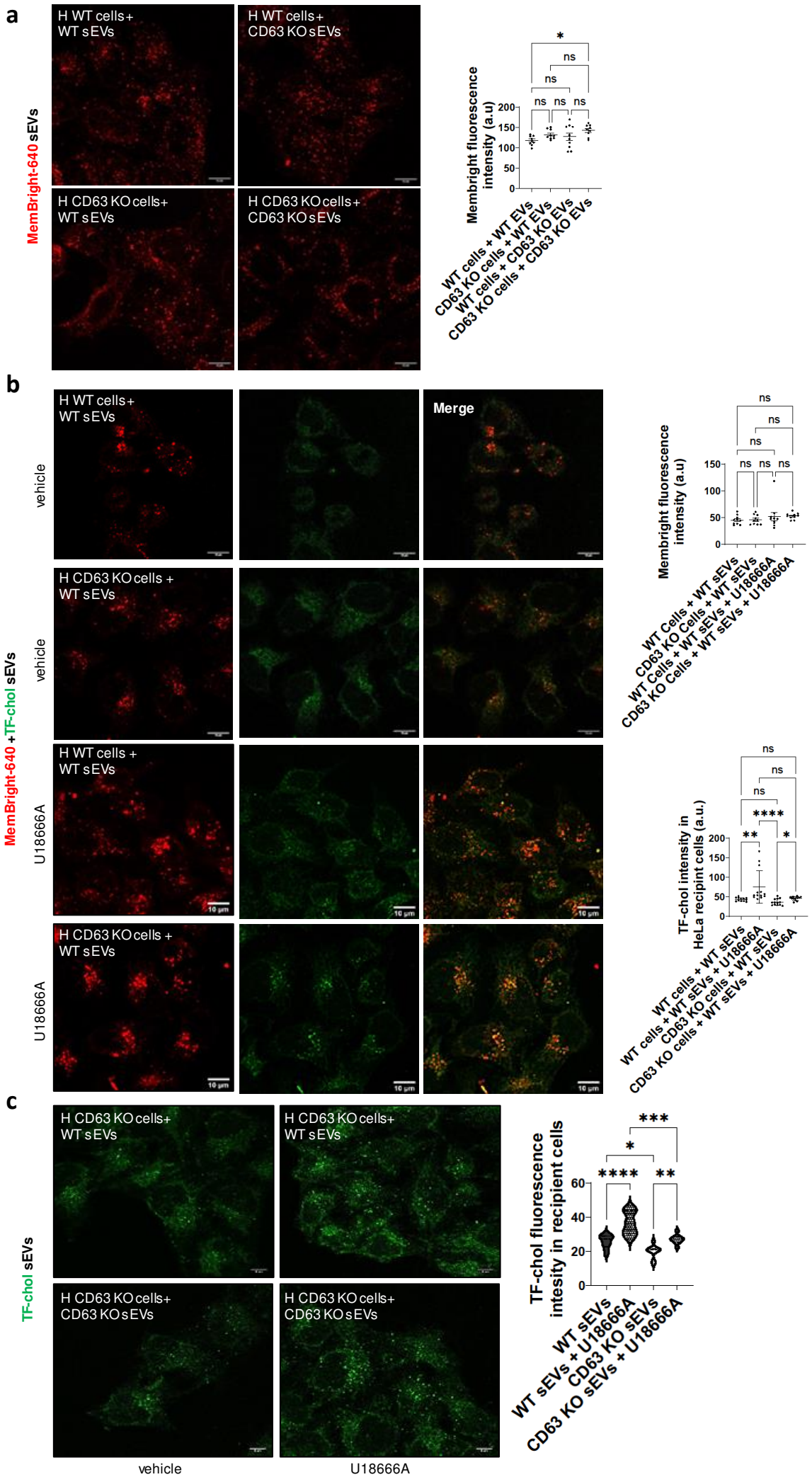
a
MemBright-640 sEVs
H WT cells+ WT sEVs
H WT cells+ CD63 KO sEVs
H CD63 KO cells+ WT sEVs
H CD63 KO cells+ CD63 KO sEVs
Membright fluorescence intensity (a.u)
WT cells + WT EVs
CD63 KO cells + WT EVs
WT cells + CD63 KO EVs
CD63 KO cells + CD63 KO EVs
b
MemBright-640 +TF-chol sEVs
vehicle
U18666A
H WT cells+ WT sEVs
Merge
H CD63 KO cells + WT sEVs
H WT cells + WT sEVs
H CD63 KO cells + WT sEVs
Membright fluorescence intensity (a.u)
WT Cells + WT sEVs
CD63 KO Cells + WT sEVs
WT Cells + WT sEVs + U18666A
CD63 KO Cells + WT sEVs + U18666A
TF-chol intensity in HeLa recipint cells (a.u.)
WT cells + WT sEVs
WT cells + WT sEVs + U18666A
CD63 KO cells + WT sEVs
CD63 KO cells + WT sEVs + U18666A
c
TF-chol sEVs
H CD63 KO cells+ WT sEVs
H CD63 KO cells+ CD63 KO sEVs
TF-chol fluorescence intesity in recipient cells
WT sEVs
WT sEVs + U18666A
CD63 KO sEVs
CD63 KO sEVs + U18666A
vehicle
U18666A

Extended Data Fig. 1.

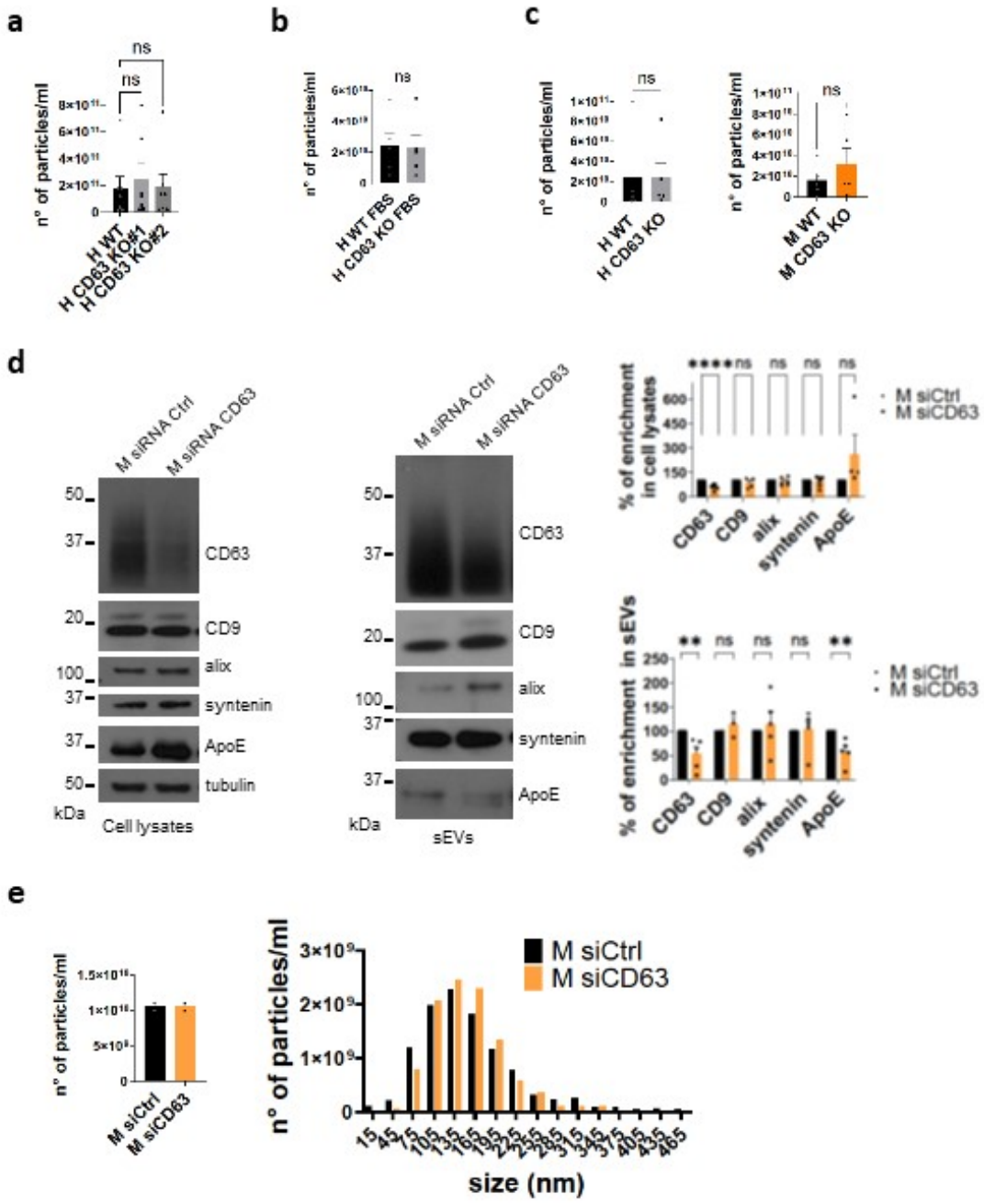

Extended Data Fig. 2

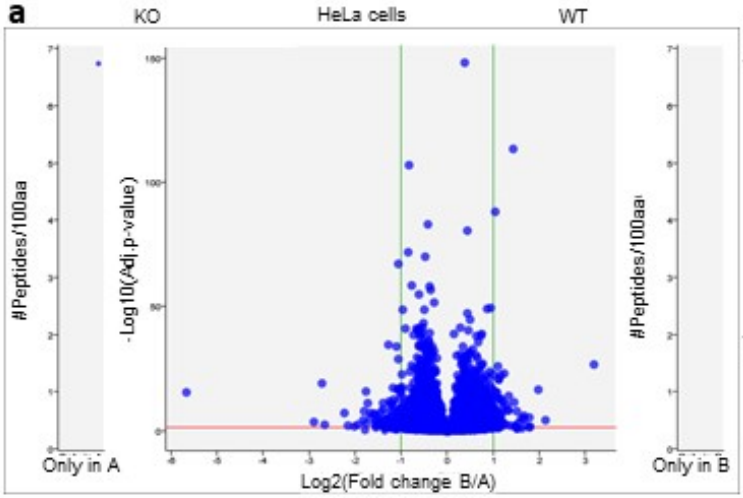

b

Name	Ratio	p-value	Description
WIPF1	9,16	1,74E-27	WAS/WASL-interacting protein family member 1
MEOX1	4,38	9,45E-05	Homeobox protein MOX-1
VTN	3,95	2,22E-17	Vitronectin
CPEB4	3,45	4,5E-06	Cytoplasmic polyadenylation element-binding protein 4
RAB6B	3,25	0,011094	Ras-related protein Rab-6B

No Cellular components Go Terms found through analysis

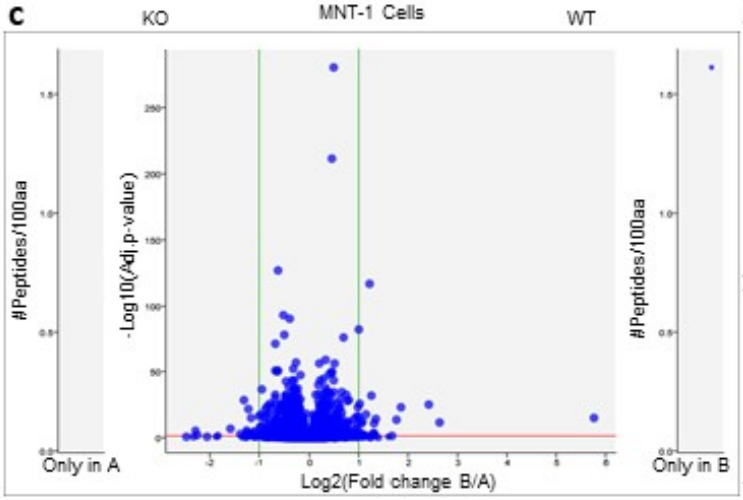

d

Name	Ratio	p-value	Description
SDCCAG3	1000	∞	Endosome-associated-trafficking regulator 1
CD63	54,45	1,11E-15	CD63 antigen
LGALS1	6,24	3,38E-12	Galectin-1
PRDX2	5,36	1,23E-25	Peroxiredoxin-2
ISYNA1	3,62	8,99E-24	Inositol-3-phosphate synthase 1

GO Term	Enrichment Factor	p-value
Membrane raft	12,27	4,60E-05
Membrane microdomain	12,231	4,67E-05
Membrane region	11,775	5,59E-05
Extracellular exosome	4,35	4,58E-06
Extracellular vesicle	4,307	5,09E-06

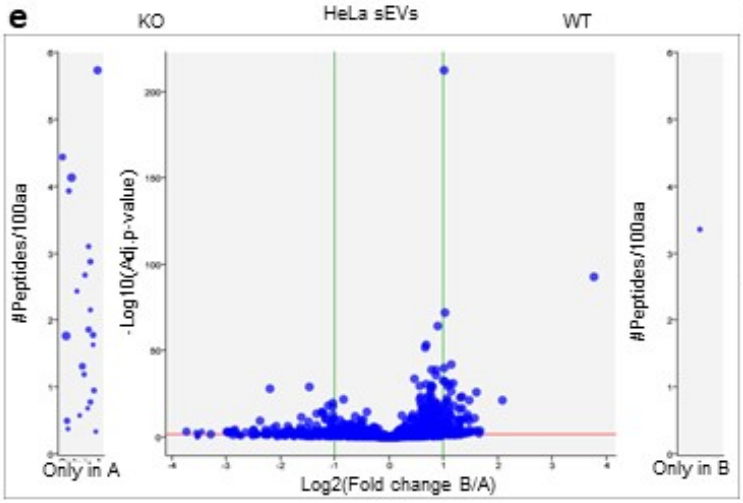

f

Name	Ratio	p-value	Description
CD63	1000	∞	CD63 antigen
MMP12	13,67	1,91E-93	Macrophage metalloelastase
BASP1	4,25	1,27E-21	Brain acid soluble protein 1
RPL29	3,19	0,00019	60S ribosomal protein L29
STMN1	3,16	0,008814	Stathmin

GO Term	Enrichment Factor	P-value
Centralspindlin complex	144,44	6,30E-05
MPP7-DLG1-LIN7 complex	86,664	2,09E-04
Extrinsic component of external side of plasma membrane	54,165	5,79E-04
Eukaryotic translation initiation factor 4F complex	33,332	1,59E-03
Microvillus membrane	28,26	1,58E-04

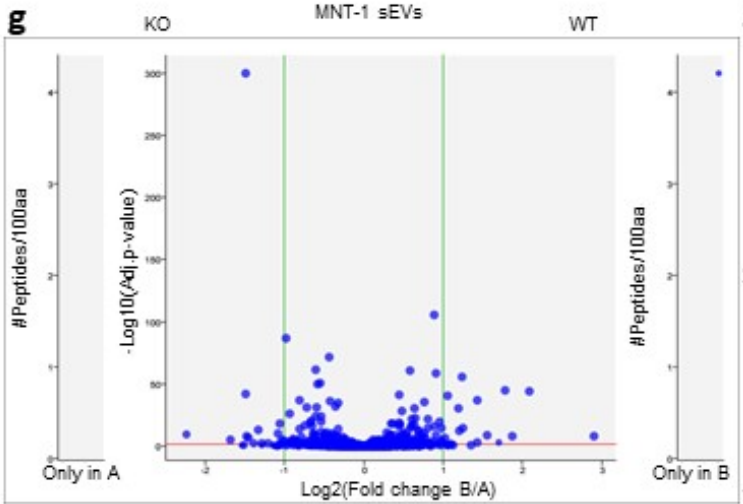

h

Name	Ratio	p-value	Description
CD63	1000	∞	CD63 antigen
GPR56	7,49	6,75E-09	Adhesion G-protein coupled receptor G1
LGALS3BP	4,26	4,05E-45	Galectin-3-binding protein
VGF	3,65	8,08E-09	Neurosecretory protein VGF
PRELP	3,44	1,01E-45	Prolargin

GO Term	Enrichment Factor	P-value
Mitochondria-associated ER Membrane	193,294	4,60E-05
Pigment granule membrane	165,681	6,33E-05
Chitosome	165,681	6,33E-05
Melanosome membrane	165,681	6,33E-05
Organelle membrane contact site	122,08	1,19E-04

Extended Data Fig. 3

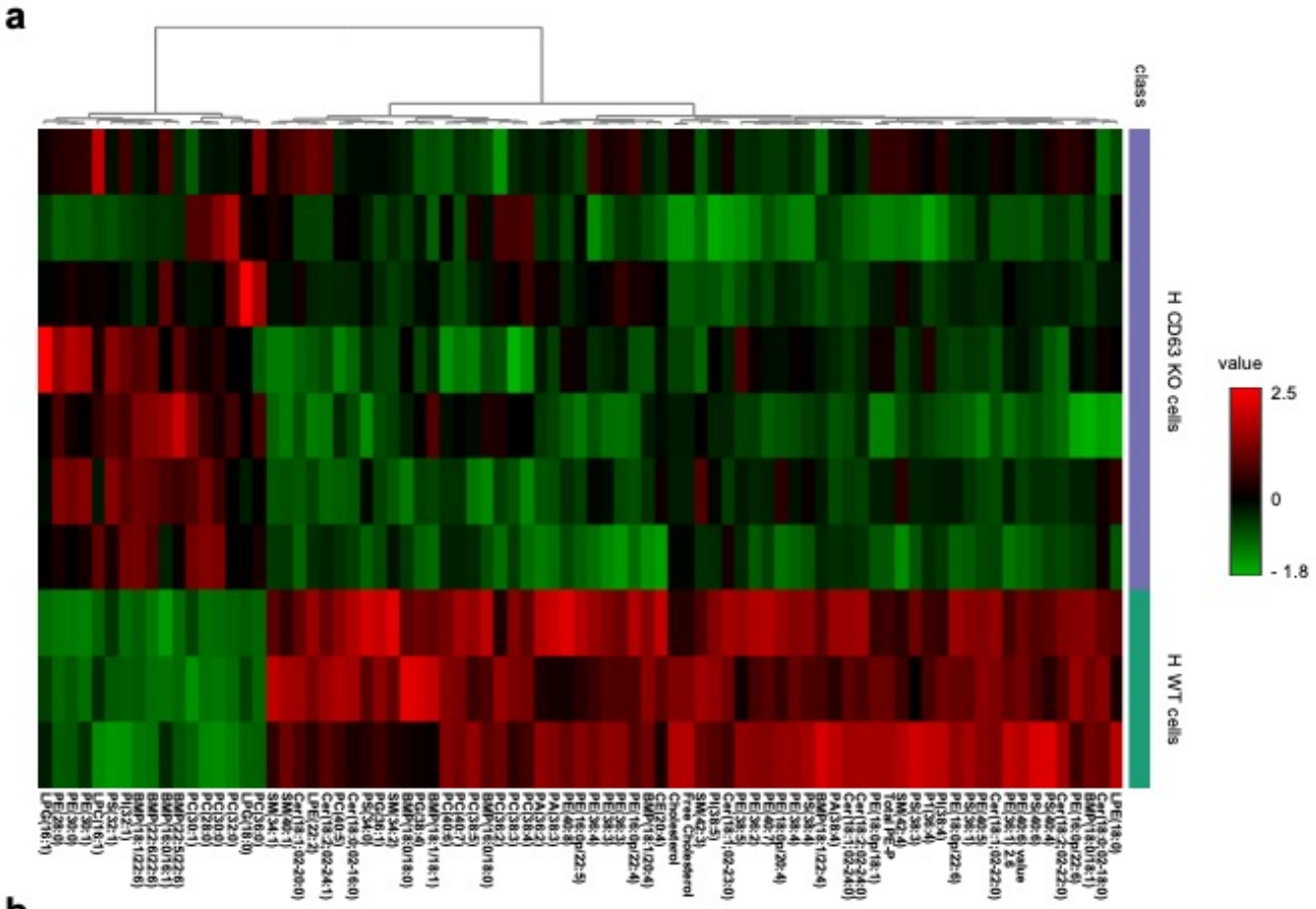

Extended Data Fig. 4

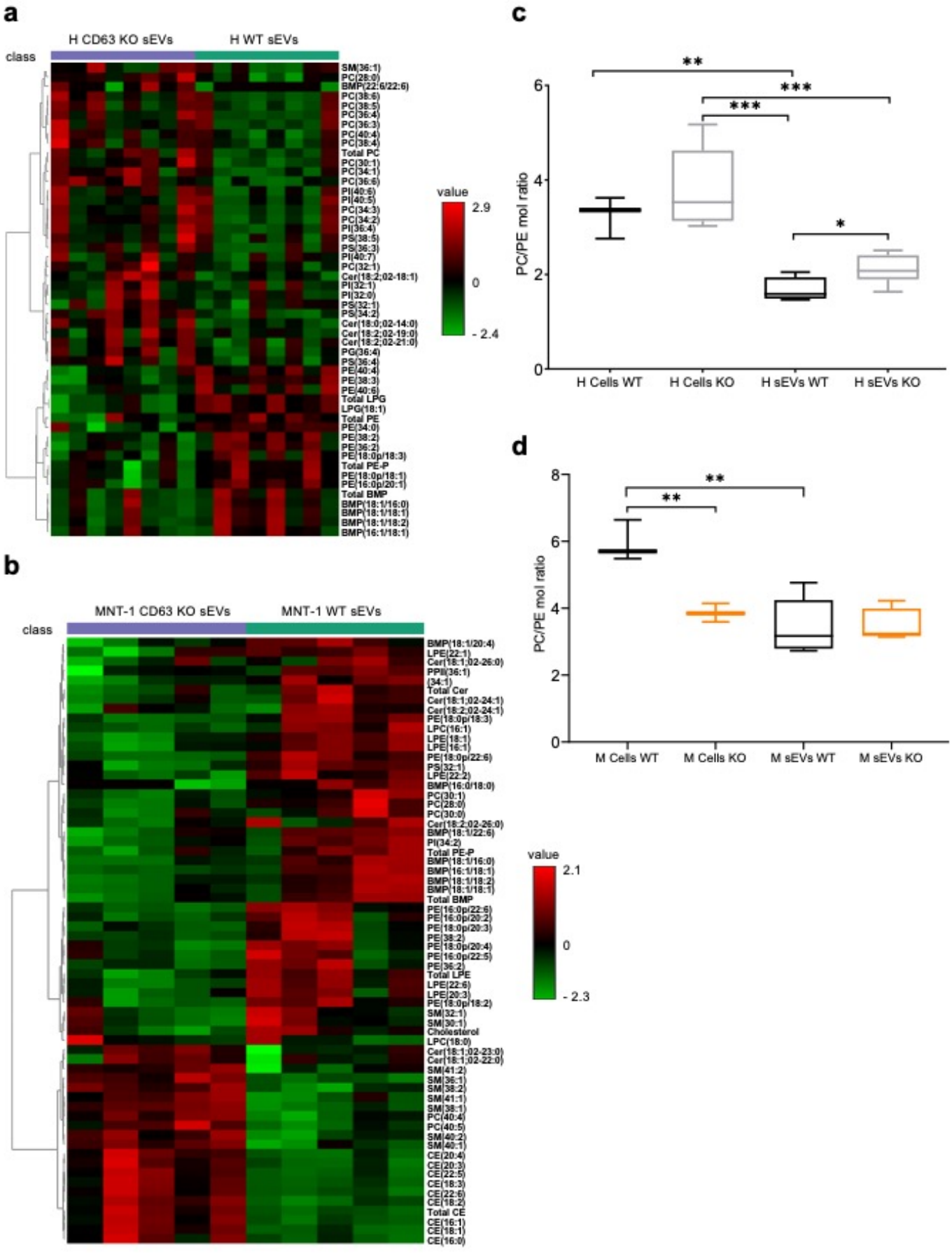

Extended Data Fig. 5

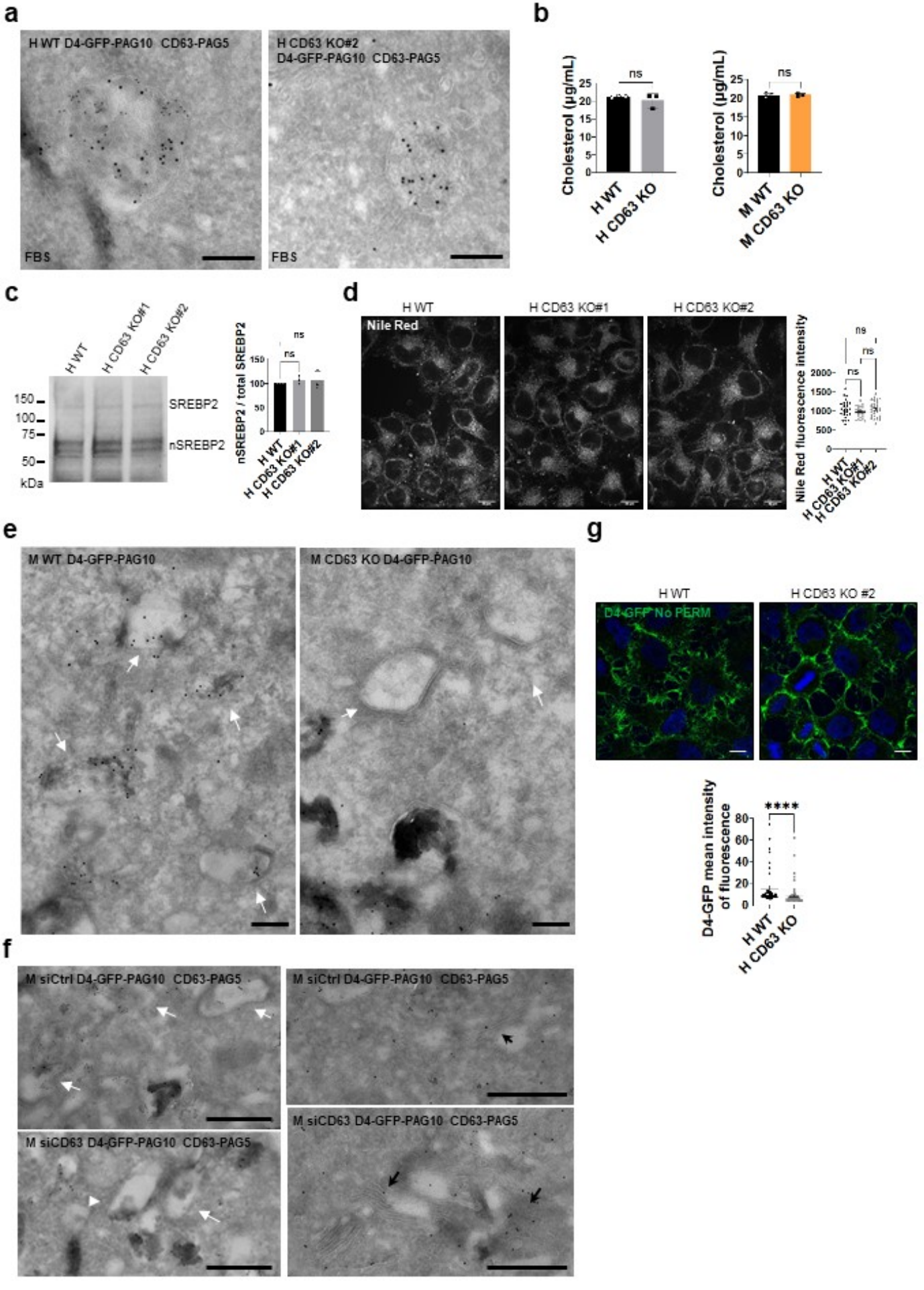

Extended Data Fig. 6

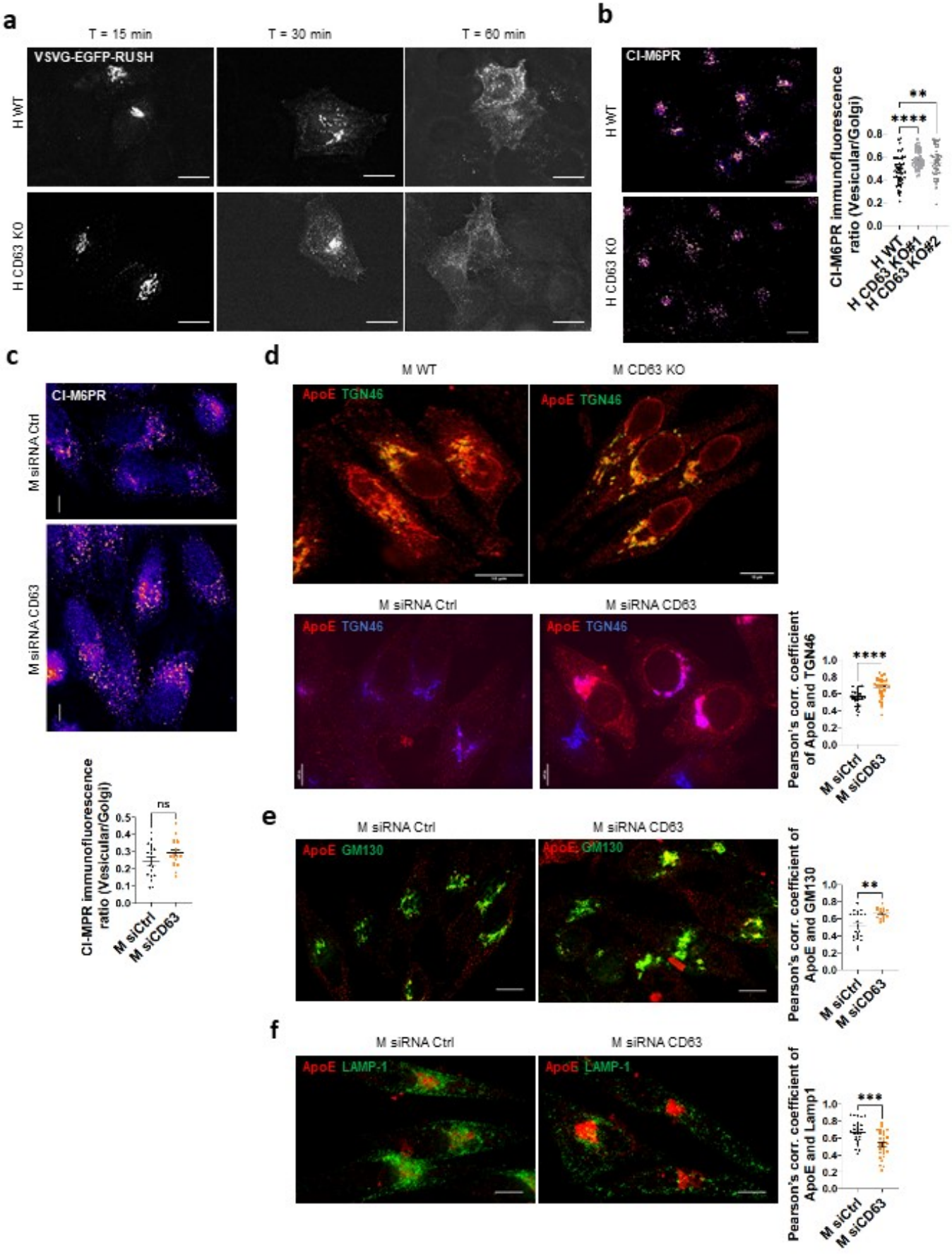

Extended Data Fig. 7

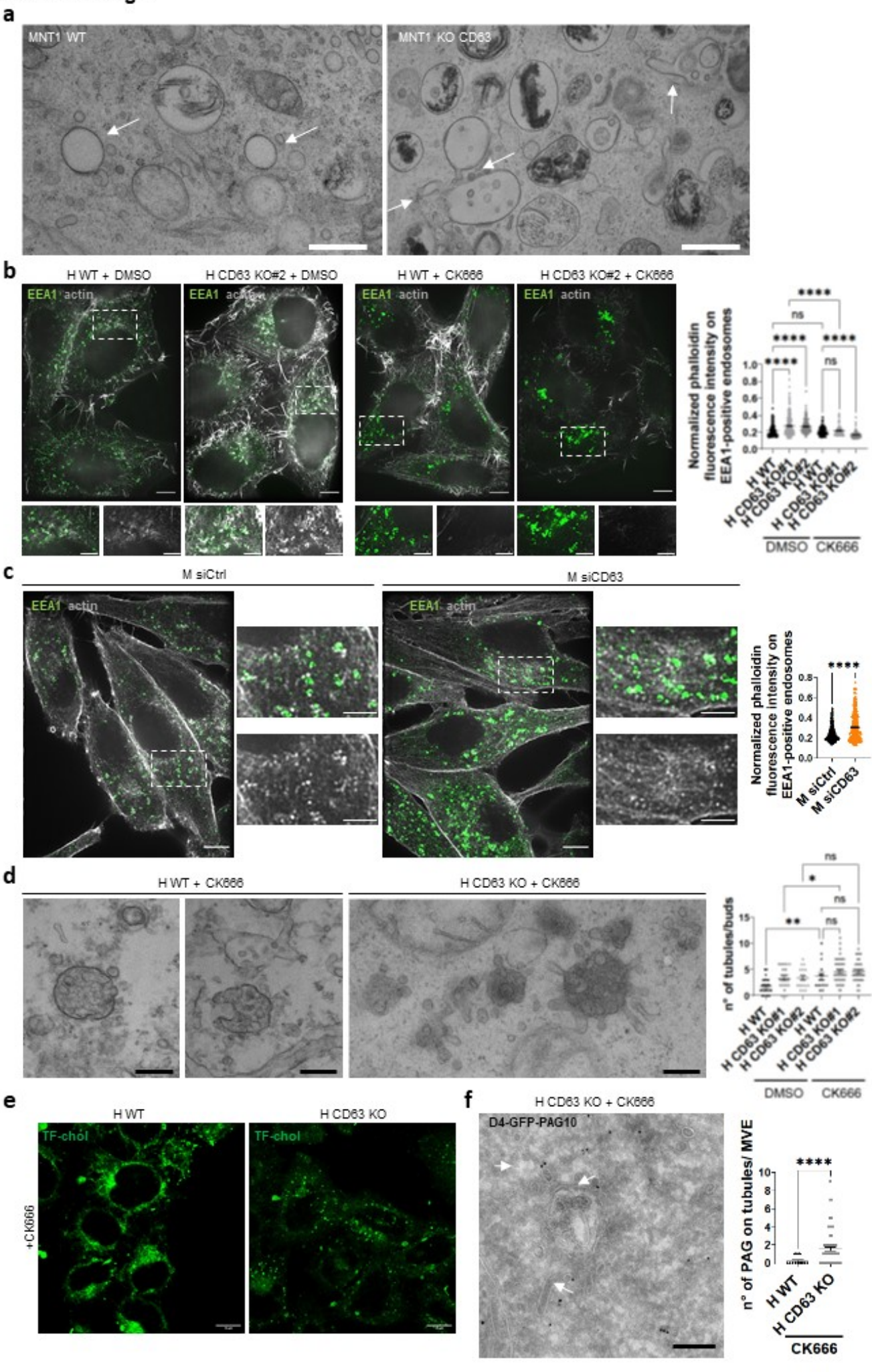

Extended Data Fig. 8

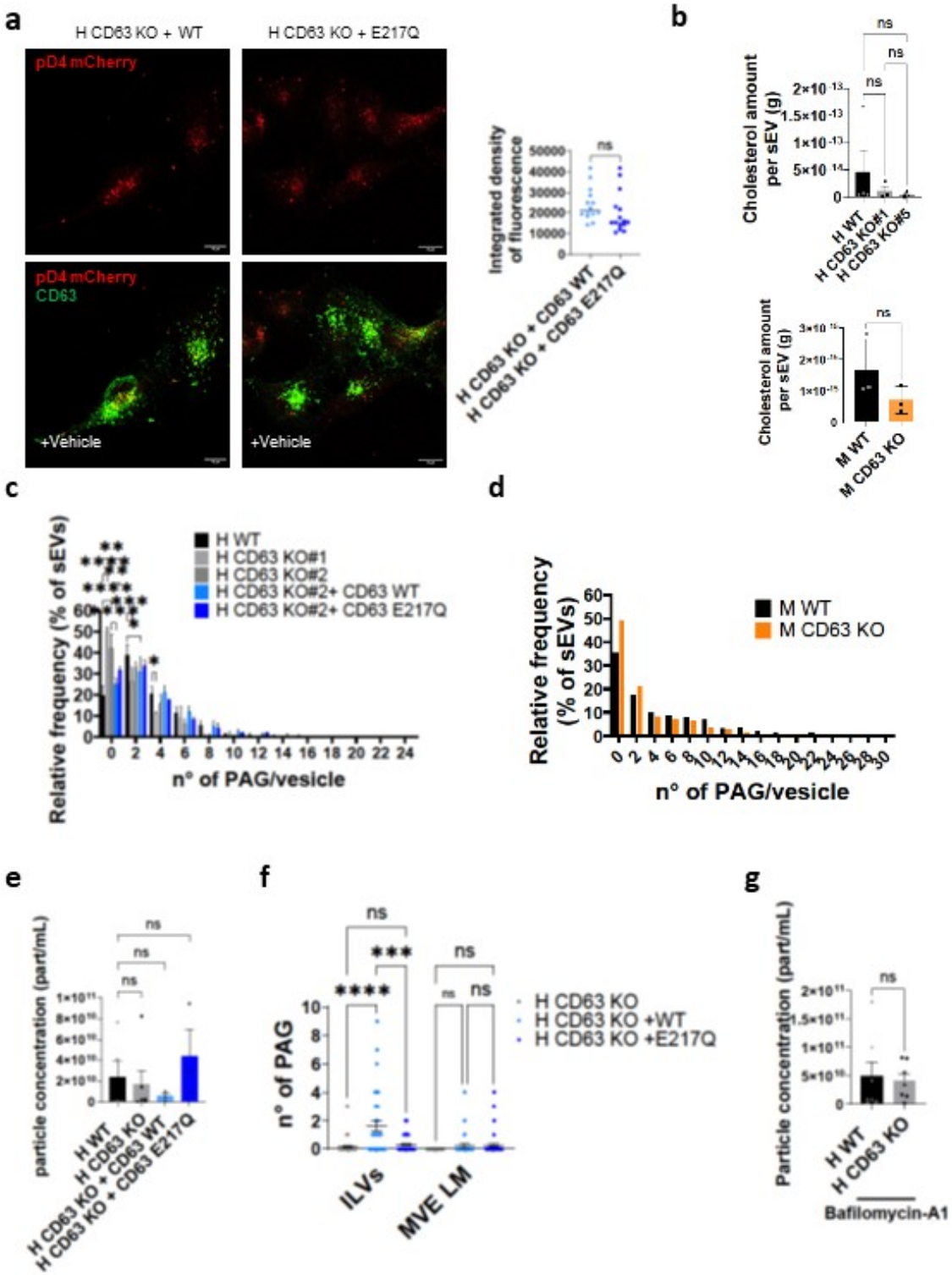

Extended Data Fig. 9